Transit regions and ejection/collision orbits in the RTBP.

M. Ollé, O. Rodríguez and J. Soler

Abstract. In this paper we analyse the global behaviour of the whole set of ejection orbits in the planar circular RTBP. We consider ejection from the big or the small primary, that is we take the mass parameter μ, the mass traditionally associated with the small primary, in a range of values $\mu \in (0, 1)$ (the other primary has mass $1 - \mu$). A discussion on the relation between the Lyapunov periodic orbit around the collinear equilibrium point L_1 and the ejection orbits is carried out in the range of values of the Jacobi constant such that the associated Hill regions permit only a bounded movement. In particular a chaotic infinity of heteroclinic connections between a primary and the LPO_1 are obtained. As a consequence a chaotic infinity of ejection-collision orbits is also derived. Finally, 2D plots, called colour code diagrams, allow to describe the global dynamics of the ejection orbits given a range of time. Such diagrams provide a very accurate understanding of the dynamics of the orbits under discussion.

1 Introduction

This paper considers the planar circular Restricted three-body problem (RTBP), which consists in describing the motion of a particle submitted to the gravitational forces of two point massive bodies (called primaries P_1 and P_2) that describe circular orbits around their common centre of mass. It is well known that in a suitable system of coordinates the motion of the particle is described by a system of ODE (given in Section 2). Such a system has a first integral, the so called Jacobi first integral, and we will denote by C the constant value along each solution. Moreover the system has five equilibrium points: the so called collinear ones L_i, $i = 1, 2, 3$ and the triangular ones L_i, $i = 4, 5$.

Although the RTBP has been extensively studied as inspiration for many theoretical analysis and numerical simulations (even as a first approximation model in different real missions), this problem is very rich from the dynamics point of view and it is far from being well understood.

In this paper we focus on the so called ejection (collision) orbits, that is orbits described by the particle that starts ejecting from a primary. It is well known that an ejection (collision) between the particle and a primary is a singularity of the system of ODE governing the motion of the particle. So a regularization strategy is required to remove the singularities and obtain a regular system of ODE. Several approaches can be done (see [7], [9], [29] and [30]) but from the computational point of view, Levi-Civita regularization proves to be a good choice.

At this point two remarks must be done: (i) the Levi-Civita regularization is done for a given fixed value of C. (ii) It is a local regularization that removes one singularity (and the other one remains).

This implies that when following the trajectory of a particle that visits a region around (or collides with) each primary, then we need to apply one regularization or the other one depending on the region the particle moves in. So the numerical integration of three different system of ODE (around each primary and far from each of them with the usual synodical variables and time) is required. In particular, with this strategy we can consider not only ejection (collision) orbits but also, ejection-collision (EC) orbits, that is trajectories where the particle ejects from a primary and after an excursion collides with a primary (which can be or not the same one).

In this context a natural definition in the literature is the so called n-EC orbit, that is, a trajectory that ejects from a primary and after n far passages (maxima in the distance with respect to that primary) collides with it.

We mention the analytical papers [6], [14] and [15] devoted to the existence of EC orbits in the particular case $n = 1$. Even some partial results are provided in the planar elliptic case, [17], and [27], and in the the spatial RTBP, [16]. And concerning numerical results, in [4], [10] and [11] the authors compute some particular EC orbits that appear when doing the continuation of families of periodic orbits.

However, dealing with the n-EC orbits for $n > 1$, as far as we know, only few papers can be mentioned. On the numerical side, [23] and [24], where the authors compute, analyse and describe the continuation of families of n-EC orbits for $n = 1, ..., 25$ and do compare the pros and cons of taking into account the Levi-Civita regularization versus the McGehee's one.

Concerning the analytical proof of existence of families of n-EC orbits for $n > 1$, the only paper we know of is [25], where, by means of a perturbative approach and using the Levi-Civita regularization, the authors prove the existence of four families for the mass parameter $\mu > 0$ small enough and C big enough.

From the point of view of astronomical applications, a great variety of papers including ejection orbits appear. Typically such papers consider just a particular value of the mass parameter. Just to mention a few, ejection orbits allow to explain a mechanism of transfer of mass in binary stars systems (see [12], [19], [28] and [31]), or to analyse regions of capture of irregular moons by giant planets (see [1]) or to study temporary capture (see most recently [26] and references therein), or the formation of Kuiper -belt binaries by means of multiple encounters with low-mass intruders (see [2]).

A different approach regarding the probability of crash motion when taking into account a big set of initial conditions and a particular range of time for a μ given and varying C is analysed in [20] and [21]. We do observe that ejection/collision orbits also play an important role in other physical problems rather than astronomy or celestial mechanics. For example in atomic physics, we mention the hydrogen atom submitted to a circularly polarized microwave field, where the ejection collision orbits (in this case between the electron and the nucleus) allow to explain a mechanism for ionization. See [5] and [22].

In this paper, we want to analyse numerically the behaviour (evolution) of the whole set of ejection orbits, which can be EC orbits or not, for a finite range of time, for a μ given and a value of the Jacobi constant C. So the starting initial condition is always ejection from a primary. Actually this analysis is done for any value of $\mu \in (0, 1)$, that is, we consider the both cases: ejecting either from the big or small primary.

More precisely, let us denote C_{L_i} the value of the Jacobi constant at the equilibrium point L_i of the system of ODE (given in Section 2). We will take $C \in [C_{L_{2,3}}, C_{L_1})$, where $C_{L_{2,3}}$ refers to C_{L_2} if $\mu \in (0, 0.5]$ (the equilibrium point L_2 is located on the left hand side of the small primary on the negative x-axis) and to C_{L_3} if $\mu \in [0.5, 1)$ (the equilibrium point L_3 is located on the right hand side of the small primary on the positive x-axis). The reasons for that choice are the following: for bigger values of C, the bounded Hill's regions of motion (where the motion of the particle is possible) are simply two close circle-like shaped regions, each one around each primary, so no possible interaction or transit from the region around one primary and the region around the other primary is possible, and the ejection orbits are pretty simple. However, for any $C \in [C_{L_{2,3}}, C_{L_1})$, the Hill's region allows to move from a region around one primary to a region around the other one. Moreover, there exists a Lyapunov periodic orbit around L_1, denoted by LPO_1. This periodic orbit and its invariant stable and unstable manifolds will play an essential role, not only to explain transition between the two regions, but also, to find infinities of heteroclinic orbits connecting the ejection and the periodic orbit, on one hand, to compute also infinities of EC orbits, on the other hand, and moreover, infinities of homoclinic orbits to the LPO_1. The interaction among these infinities, and the effects on the ejection orbits result in a chaotic classification of the dynamical behaviour of the ejection orbits. We also remark that other periodic orbits in this same level of fixed C exist and do interfere with the ejection orbits. For smaller values of $C < C_{L_{2,3}}$, the Hill's region allows to connect the ejection with the infinity and there appear other Lyapunov and other kind of periodic orbits and, therefore, the dynamics gets much more complicated.

So, focussed on the description of the behaviour of the ejection orbits, our main goal on this paper is threefold: *first*, to describe big sets of ejecting orbits from one primary that transit to the region around the other primary. A key role in this transition is played by the heteroclinic connections between one primary and the LPO_1, denoted by $P_i - LPO_1$, $i = 1$ or 2. Two main important consequences are explained: such heteroclinic connections act as barriers of transition regions and, moreover, allow to classify the geometrical trajectory of the ejection (collision) orbits. *Second*, although in principle the classification seems clear to apply, we show that this is not the case at all, due to the existence of a chaotic infinity of heteroclinic connections $P_i - LPO_1$. We explain how this chaotic infinity is generated. *Third*, for a $\mu > 0$ given and C fixed, we want to visualize the trajectory that an ejection orbit will describe for a finite range of time, for any ejection orbit. That is, the key point is that this description will be done by means of 2D colour code diagram plots, which contain the global dynamics of the whole set of individual ejection orbits. All the ingredients described before appear in these meaningful 2D plots that provide a global perspective.

The paper is organized in such a way that the complexity of the dynamical phenomena analysed along the paper is progressively described. In Section 2, we recall some properties of the planar circular RTBP, that will be used along the paper. Section 3 is devoted to the Levi-Civita regularization. Although it is well known in the literature, we recall the system of ODE obtained with these Levi-Civita variables and suitable time. So Sections 2 and 3 provide the necessary preliminaries to start all the numerical simulations and we can deal with any ejection/collision with either one of the primaries. We also provide the initial conditions for ejection/collision orbits. We will show that, fixed μ and C, an ejection orbit is determined simply by an initial angle denoted by $\theta_0 \in [0, \pi)$. In Section 4 and 5, we discuss the role of the Lyapunov periodic orbit LPO_1 and its stable and unstable manifolds and their interaction with the ejection orbits. A first effect of this interaction is that the existence of heteroclinic connections $P_1 - LPO_1$ allows to classify (for a finite range of time) the trajectory described by one ejection orbit. This classification will take into account two properties: if the particle (that ejected from P_1) describes a number n of close approaches to that primary and if it visits the region around the other primary P_2 (we will say a transit orbit) or if it does not and remains on the same region around P_1 (a non transit orbit). We will show that the barrier that separates transit and non transit orbits will be given by the heteroclinic connections $P_1 - LPO_1$, that is, by intervals of values of θ_0, called transition intervals, whose end points are specific values of angles θ_0 corresponding to heteroclinic connections. As a first simple description, we discuss big transition intervals. However, this simple description is apparent since the existence of infinitely many heteroclinic connections make the discussion of transition intervals much more involved. So in Section 4, besides big transition intervals, we also introduce the effect of a finite number of heteroclinic connections. Once this effect is explained, Section 5 is aimed at the generalization of the previous discussion: there appears not a finite number of heteroclinic connections but but a chaotic infinity of heteroclinic connections $P_i - LPO_1$. Now the discussion is more intricate. We explain the mechanism to generate such infinity which relies in particular on the existence of (also infinitely many) homoclinic orbits to the LPO_1. Another relevant consequence of such infinities is that there is also a chaotic infinity of ejection collision (EC) orbits. The generation of such EC orbits is also discussed in Section 5. So far, the main ingredients that explain the rich phenomena concerning the dynamical behaviour of the ejection orbits is accomplished. Finally the purpose of Section 6 is to provide a 2D plot which contains the dynamical behaviour (for a finite range of time) of the whole set of ejection orbits, for the mass parameter $\mu \in (0, 1)$ and C given. We call such 2D plot as *colour code diagram plot*. Such plot can be regarded as a *global picture of the ejection dynamics*. Therefore the results described in Sections 4 and 5 are collected and are visible in such 2D plots.

We end the paper drawing some conclusions.

Finally, we remark that all the computations have been done using double precision and the numerical integration of the systems of ODE has been done using an own implemented Runge-Kutta (7)8 integrator with an adaptive step size control described in [8] and a Taylor method implemented on a robust, fast and accurate software package in [13].

2 The planar RTBP

We describe some properties of the RTBP which are necessary for the remaining part of the paper.

As it is well known, the goal of the planar circular, restricted three-body problem (RTBP) is to analyse the motion of a particle of infinitesimal mass, that moves on the same plane and under the gravitational influence of two massive bodies P_1 and P_2, called primaries, that are assumed to describe circular orbits around their common centre of mass (located at the origin). In order to deal with an autonomous system of ordinary differential equations, it is quite common to consider (i) a system of coordinates (x, y) that rotates with the primaries (called rotating or synodical system), and (ii) suitable units of time, mass and length such that the primaries have masses $1-\mu$ and μ, $\mu \in (0, 0.5]$, their positions are fixed at $(\mu, 0)$ and $(\mu - 1, 0)$, respectively, and the period of their motion is 2π. We remark that typically, since μ is taken in $(0, 0.5]$, the big primary is located on the positive x axis and the small one on the negative x axis. However in this paper we will extend the value of $\mu \in (0, 1)$, so for $\mu \in (0.5, 1)$, the location of the primaries changes to the opposite side. With these assumptions, the equations of motion for the particle in the synodical system are given by

$$\begin{cases} \ddot{x} - 2\dot{y} = \Omega_x(x, y) \\ \ddot{y} + 2\dot{x} = \Omega_y(x, y), \end{cases} \tag{1}$$

where $\dot{} = d/dt$ and

$$\begin{aligned} \Omega(x, y) &= \frac{1}{2}(x^2 + y^2) + \frac{1-\mu}{\sqrt{(x-\mu)^2 + y^2}} + \frac{\mu}{\sqrt{(x-\mu+1)^2 + y^2}} + \frac{1}{2}\mu(1-\mu) \\ &= \frac{1}{2}\left[(1-\mu)r_1^2 + \mu r_2^2\right] + \frac{1-\mu}{r_1} + \frac{\mu}{r_2} \end{aligned} \tag{2}$$

with $r_1 = \sqrt{(x-\mu)^2 + y^2}$ and $r_2 = \sqrt{(x-\mu+1)^2 + y^2}$. So, the equations become singular when r_1 or $r_2 \to 0$. The crucial aim of this paper is to study the orbits that eject or collide with one primary, that is $r_1 = 0$ or $r_2 = 0$.

We also shortly recall the following properties of system (1) (see [30] for details)

1. There exists a first integral, known as Jacobi integral, defined as
$$C = 2\Omega(x, y) - \dot{x}^2 - \dot{y}^2 \tag{3}$$
2. The equations of motion satisfy a reversibility
$$(t, x, y, \dot{x}, \dot{y}) \to (-t, x, -y, -\dot{x}, \dot{y}). \tag{4}$$
This can be viewed as a geometrical symmetry: for any solution $(x(t), y(t), \dot{x}(t), \dot{y}(t))$ of (1), forward in time, there exists another solution, backwards in time, $(x(-t), -y(-t), -\dot{x}(-t), \dot{y}(-t))$. So, given a trajectory for the particle in the configuration space (x, y), there exists another one which is symmetric with respect to the x axis. We remark that there is an additional obvious symmetry when $\mu = 0.5$, that is the two primaries have equal mass.

3. System (1) has the well known 5 equilibrium points: the collinear ones L_i, $i = 1, 2, 3$, and the triangular ones L_i, $i = 4, 5$. On the plane (x, y), $L_{1,2,3}$ are located on the x axis, with $x_{L_2} < \mu - 1 < x_{L_1} < \mu < x_{L_3}$ and $L_{4,5}$ forming an equilateral triangle with the primaries. We will keep this notation for any value of $\mu \in (0, 1)$.

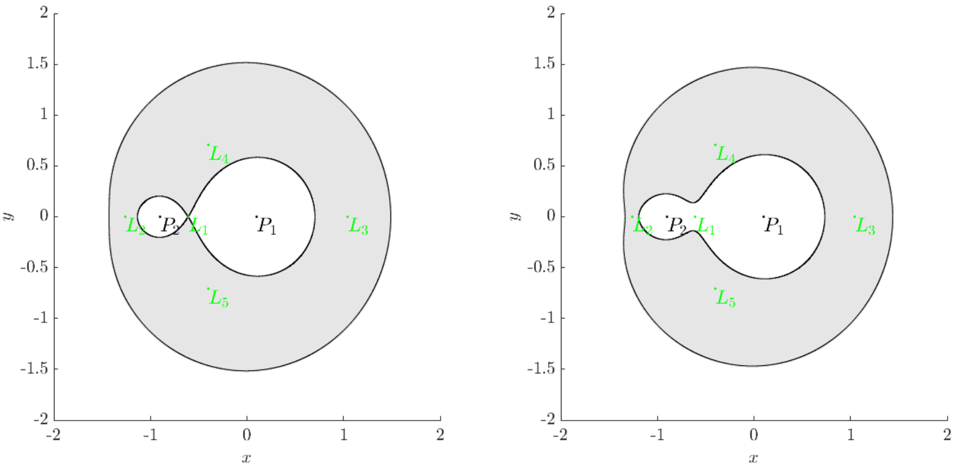

Figure 1: Hill regions for $C = C_{L_1}$ (left) and for $C_{L_2} < C < C_{L_1}$ (right).

4. From the Jacobi integral and taking into account that $2\Omega(x, y) - C \geq 0$, given a value of the Jacobi constant C, the motion can only take place in the Hill's region defined by

$$\mathcal{R}(C) = \left\{(x, y) \in \mathbb{R}^2 \,|\, 2\Omega(x, y) \geq C\right\}. \tag{5}$$

We denote by C_{L_i} the value of C at L_i, $i = 1, ..., 5$, and it is also known that the topology of the Hill's regions vary with C_{L_i}. In this paper we will consider the range of $C \geq C_{L_{2,3}}$. We show in Figure 1 the topology of the Hill's regions considered.

5. Applying Lyapunov's Theorem (see [18]), it is well known that for $C < C_{L_i}$, $i = 1, 2, 3$ there exists a one parameter family of periodic orbits, called Lyapunov periodic orbits around L_i, $i = 1, 2, 3$, and parametrized by C. We will denote by LPO_i, $i = 1, 2, 3$ the associated Lyapunov periodic orbit for a given suitable C.

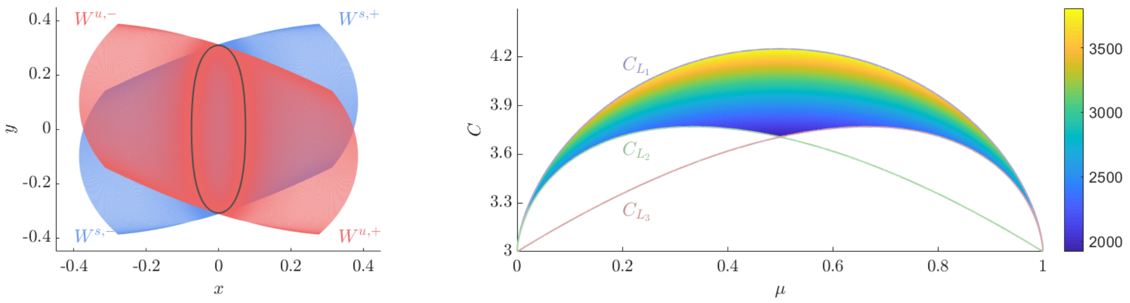

Figure 2: *Left.* Branches $W^{u,\pm}$ and $W^{s,\pm}$ of a LPO_1; projection (x, y). *Right.* Maximum eigenvalue of the monodromy matrix (in colour) when varying $\mu \in (0, 1)$ and $C \in [C_{L_{2,3}}, C_{L_1})$.

A natural question that arises is if there is a relation between the LPO_i and the ejection/collision orbits. The answer is definitely yes, the ejection/collision orbits may have different kind of trajectories explained because of the invariant manifolds of the LPO_i. To illustrate it we will consider the range

$C \in [C_{L_{2,3}}, C_{L_1})$ and study the periodic orbit LPO_1, its invariant manifolds and their interaction with the ejection/collision orbits. An immediate consequence of this interaction is that ejection orbits eject from one primary, get close to the LPO_1 and do transit to the region around the other primary or do not and bounce back to the same region of the primary the particle ejected from. This is a crucial point on this paper.

Going into detail, recall that to determine the stability/instability of a periodic orbit, we just need to compute the eigenvalues of the monodromy matrix (the fundamental matrix of the variational equations along the periodic orbit up to a period). It is also well known that the LPO_i are unstable (such eigenvalues are 1, 1, λ, $1/\lambda$, with $\lambda > 1$) at least for a suitable range of C close to C_{L_i}, $i = 1, 2, 3$. Applying the theorem of stable/unstable manifolds (see for example [18]), the existence of 2D invariant manifolds associated with each LPO_i is guaranteed. We will focus on the LPO_1 and will discuss how the associated 2D invariant manifolds explain why orbits that eject from one primary remain on the same region or visit a region around the other primary. We will denote by $W^{u,+}$, $W^{u,-}$ (similarly $W^{s,+}$, $W^{s,-}$) the branches of the unstable (stable) manifolds that *start* asymptotically forward (backward) in time on the right or left hand side of the periodic orbit respectively (see Figure 2); we will call them positive and negative branch respectively. As already mentioned we will consider the range of values of $C \in [C_{L_{2,3}}, C_{L_1})$, so only the periodic orbit LPO_1 and its associated manifolds will be taken into account. Such orbit is highly unstable; we plot in Figure 2 the maximum real eigenvalue $\lambda > 1$ of the LPO_1 for any value of $\mu \in (0, 1)$ (on the x axis) and the range $C \in [C_{L_{2,3}}, C_{L_1})$ (on the y axis). We remark that such eigenvalue is large (approximately between 2000 and 4000) for all $\mu \in (0, 1)$.

3 The Levi-Civita regularization and ejection/collision orbits

3.1 Levi-Civita regularization

In order to deal with the singularity of the each primary ($r_1 = 0$ or $r_2 = 0$) we must consider a regularization of the system of ODE to transform such singularities to regular points. Different possibilities may be taken into account: either global regularizations (that regularize both collisions with the primaries) or local ones (only regularizes one of them). We have chosen the local option because it is more efficient from the numerical point of view, and our purpose on this paper is to do massive numerical simulations. Even, within the local option, there are different possibilities. We refer to [24] for a discussion between McGehee's and Levi-Civita's choices. The main conclusion of that paper is that, from a numerical point of view, Levi-Civita is the best choice. So along the paper we consider Levi-Civita (local) regularization that allows to transform the singular system of ODE to a regular one (locally around each of the primaries). The well known transformation of coordinates and time (see [30]) is given by:

$$\begin{cases} x = a + u^2 - v^2 \\ y = 2uv \\ \dfrac{dt}{ds} = 4\left(u^2 + v^2\right) \end{cases} \tag{6}$$

where $a = \mu$ or $a = \mu - 1$ in order to regularize the collision with the primary P_1 or P_2 respectively. The system (1), regularizing the collision with the primary P_1, becomes:

$$\begin{cases} u'' - 8(u^2+v^2)v' = \big(4U(u^2+v^2)\big)_u \\ \qquad\qquad = 4\mu u + 16\mu u^3 + 12(u^2+v^2)^2 u + \dfrac{8\mu u}{r_2} - \dfrac{8\mu u(u^2+v^2)(u^2+v^2+1)}{r_2^3} - 4Cu \\ v'' + 8(u^2+v^2)u' = \big(4U(u^2+v^2)\big)_v \\ \qquad\qquad = 4\mu v - 16\mu v^3 + 12(u^2+v^2)^2 v + \dfrac{8\mu v}{r_2} - \dfrac{8\mu v(u^2+v^2)(u^2+v^2-1)}{r_2^3} - 4Cv \\ C' = 0 \end{cases} \tag{7}$$

where $' = d/ds$ and

$$U = \frac{1}{2}\left[(1-\mu)\left(u^2+v^2\right)^2 + \mu\left((1+u^2-v^2)^2 + 4u^2v^2\right)\right] + \frac{1-\mu}{u^2+v^2} + \frac{\mu}{r_2} - \frac{C}{2}.$$

with $r_2 = \sqrt{(1+u^2-v^2)^2 + 4u^2v^2}$. The system of ODE is now regular everywhere except at the collision with the small primary ($r_2 = 0$). Similarly we obtain the corresponding system of ODE regularizing the collision with the primary P_2 (not written explicitly on the paper).

We remark that the system of ODE (7) makes sense for each value of a Jacobi constant C fixed. So, in order to take an initial condition of this system, we will take $(u(0), v(0), u'(0), v'(0), C(0))$. However, for all the coming computations we will actually consider system (7) removing the last equation in C, and we will consider the corresponding solution for a fixed C and initial condition given simply by $(u(0), v(0), u'(0), v'(0))$.

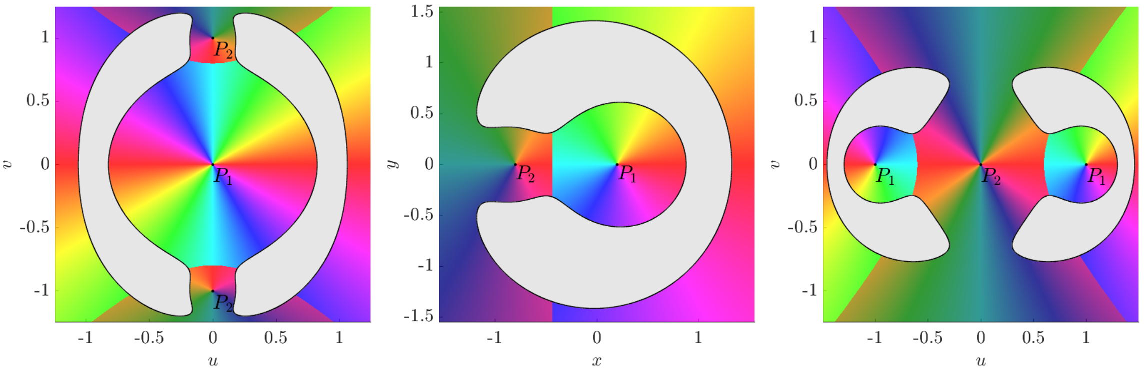

Figure 3: $C = 3.53$ $\mu = 0.2$, Hill's region in Levi-Civita coordinates (u, v) regularizing the collision with P_1 (left), regularizing the collision with P_2 (right) and in synodical (x, y) coordinates. The light gradient of colours represents the angle with respect to the position of the first primary (for $x \geq x_{L_1}$) and the dark gradient represents the angle with respect the second primary (for $x < x_{L_1}$) in the synodical coordinates. As we can see, the configuration space is doubled.

In this system of reference, the previous properties of the RTBP are written correspondingly (see [25] for details). Just let us mention that each point in (x, y) coordinates is mapped to two points in (u, v) coordinates (see Figure 3) and the equations of motion in Levi-Civita variables satisfy the following symmetries:

$$(s, u, v, u', v') \to (s, -u, -v, -u', -v') \tag{8a}$$

$$(s, u, v, u', v') \to (-s, -u, v, u', -v') \tag{8b}$$

Concerning the numerical simulations, we point out two comments: (i) we typically proceed as follows: outside a small neighbourhood of each primary, we use synodical coordinates (x, y) and the usual time t. Whenever we are inside a small neighbourhood of one primary, we consider the suitable Levi-Civita coordinates (u, v) and the corresponding local time s. See Figure 4. (ii) Thus, we consider 3 different times, a global time t when working with synodical coordinates (x, y) and a variable s when dealing with the Levi-Civita coordinates, (so actually two different times depending on which local regularization we are considering). So the system of ODE in Levi-Civita coordinates that we take into account is 6-dimensional, 4 ODE for (u, v, u', v') plus 2 additional ODE on the other two additional times with respect which we do not integrate (for example if we integrate the system of ODE around the big primary, we also integrate the time t and the other time s of the regularization around the small primary). This will be specially useful in Section 6, when describing a global evolution of ejection orbits.

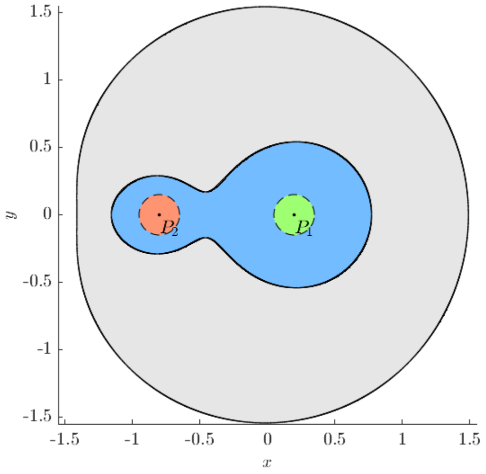

Figure 4: $\mu = 0.2$, $C = 3.8$. The motion will be considered on the blue region and in synodical (x, y) coordinates, except in a neighbourhood of each primary (green and red areas) where the corresponding Levi-Civita regularization is carried out.

3.2 Ejection/collision orbits

The key goal of this paper is to describe the dynamics of the orbits ejecting from (or colliding with) one primary.

First let us describe how we compute such orbits: given a value of μ and C, we consider Levi-Civita coordinates (u, v, u', v'), and take initial conditions at $s = 0$

$$(0, 0, u'_0, v'_0) \tag{9}$$

with $u'_0 = 2\sqrt{2(1-b)}\cos\theta_0$, $v'_0 = 2\sqrt{2(1-b)}\sin\theta_0$, varying $\theta_0 \in [0, \pi)$, where $b = \mu$ or $\mu - 1$ if we eject from P_1 or P_2 respectively, and we integrate forward (backward) in time system (7) in order to obtain the ejecting (colliding) orbits. So each ejection (collision) orbit will be identified by a value of θ_0, since its initial condition is determined from it, for C fixed. As a whole set of ejecting (colliding) orbits, varying $\theta_0 \in [0, \pi)$, we deal with a 2D manifold of ejecting (colliding) orbits. We will denote by $W^e(P_i)$ and $W^c(P_i)$, $i = 1, 2$ the corresponding 2D manifolds. We observe that we will keep the terminology of 2D manifolds (by similarity to McGehee regularization, see [24]) although in Levi-Civita variables, the collision point is a regular non equilibrium point.

At this point it is important to remark that the numerical computations along the paper will be done for $\mu \in (0,1)$, this means that we are analysing the dynamics of both cases, ejecting orbits from (colliding orbits to) the big primary (for $\mu \in (0,0.5]$) or the small primary (for $\mu \in (0.5,1)$). More precisely, when $\mu \in (0,0.5]$, the big primary is located at $(\mu,0)$ and the small one at $(\mu-1,0)$, whereas for $\mu \in (0.5,1)$, the big one is at $(\mu-1,0)$ and the small one at $(\mu,0)$. When $\mu = 0.5$, both primaries have the same mass, so the dynamics analysed with respect to one primary is exactly the same with respect to the other one.

Once we have the main setting and we are able to compute ejection (collision) orbits, a main question, as mentioned in the Introduction, arises: How do ejection orbits behave? That is, given a $\theta_0 \in [0,\pi)$, what is the trajectory of the corresponding ejection orbit? Of course this is a too ambitious question to be answered in general. But going into this goal, we will consider in this paper a first restriction that will allow us to answer this question in an easier way. It consists of considering a range of the Jacobi constant C. On one hand for $C \in [C_{L_1},\infty)$, the bounded Hill regions only allow motion around each primary so the ejection orbit only can remain on the region around the primary it ejected from. On the other hand, for $C \in [C_{L_{2,3}}, C_{L_1})$ there is the Lyapunov periodic orbit LPO_1 and its invariant manifolds which interact with the ejection orbits. The remaining sections are devoted to provide a description of the trajectory that the ejection orbit, determined by θ_0, describes for a finite range of time (taking into account essentially not only the role of the LPO_1 but also the influence of other invariant objects). This trajectory will be classified mainly by the successive transit/non transit paths from the region around the primary the particle ejected from and the region around the other primary. We will show that besides ejection-collision orbits with respect to one primary (this was a main goal in [23] and [25]), also other interesting and intricated behaviours appear.

4 Transit Regions

A main goal in this Section is to study *big* regions of ejection-transit orbits. This means big sets of orbits where the particle ejects from one primary and, in a natural way, *crosses* a Poincaré section Σ (defined by $x = const$) and goes to the region where the other primary is located. In order to somewhat classify the ejecting orbits, we will distinguish among the ejection orbits that, after describing n *close passages* around the primary P_i (from which the orbit started) cross the section Σ. Numerically, the condition of close passage means that, in the suitable Levi-Civita coordinates (depending on the primary we are regularizing), a minimum in the (square) distance u^2+v^2 is achieved so the conditions $f(\boldsymbol{u}) = uu' + vv' = 0$ and $f'(\boldsymbol{u}) > 0$ where $\boldsymbol{u} = (u, v, u', v')$, are satisfied.

In Figure 5 left, and for $\mu = 0.5$, $C = C_{L_2}$, we show in red big regions (the (x, y) projection) of ejection orbits from P_1 that after n close passages around P_1 (for $n = 0, 1, 2, 3$) cross Σ defined by $x = 0.1$.

A natural question arises: how do we find such big regions? The answer is through the heteroclinic connections between a primary and the LPO_1, denoted by $P_i - LPO_1$, $i = 1, 2$. We will call a *heteroclinic connection* $P_i - LPO_1$, $i = 1$ or 2, the orbit that ejects from P_i, $i = 1$ or 2, and ends asymptotically in the LPO_1.

So, first of all, let us compute those possible heteroclinic connections between a primary and the LPO_1, such that the particle, after ejecting from a primary, describes n close passages around it and goes directly to the LPO_1 where it ends asymptotically.

We describe how to compute a heteroclinic connection $P_1 - LPO_1$, (we proceed similarly for the other case, $P_2 - LPO_1$). Since a heteroclinic connection $P_1 - LPO_1$ is an orbit that belongs to $W^e(P_1) \cap W^s(LPO_1)$, the numerical strategy to compute such connections, given $\mu > 0$ and for a fixed value of C, consists, roughly speaking, in the following steps: to compute the 2D manifold $W^s(LPO_1)$ (one of the two possible branches) up to a given Poincaré section Σ, giving rise to a curve denoted by γ_s (see for example [3] for more details and references therein); to compute the 2D manifold

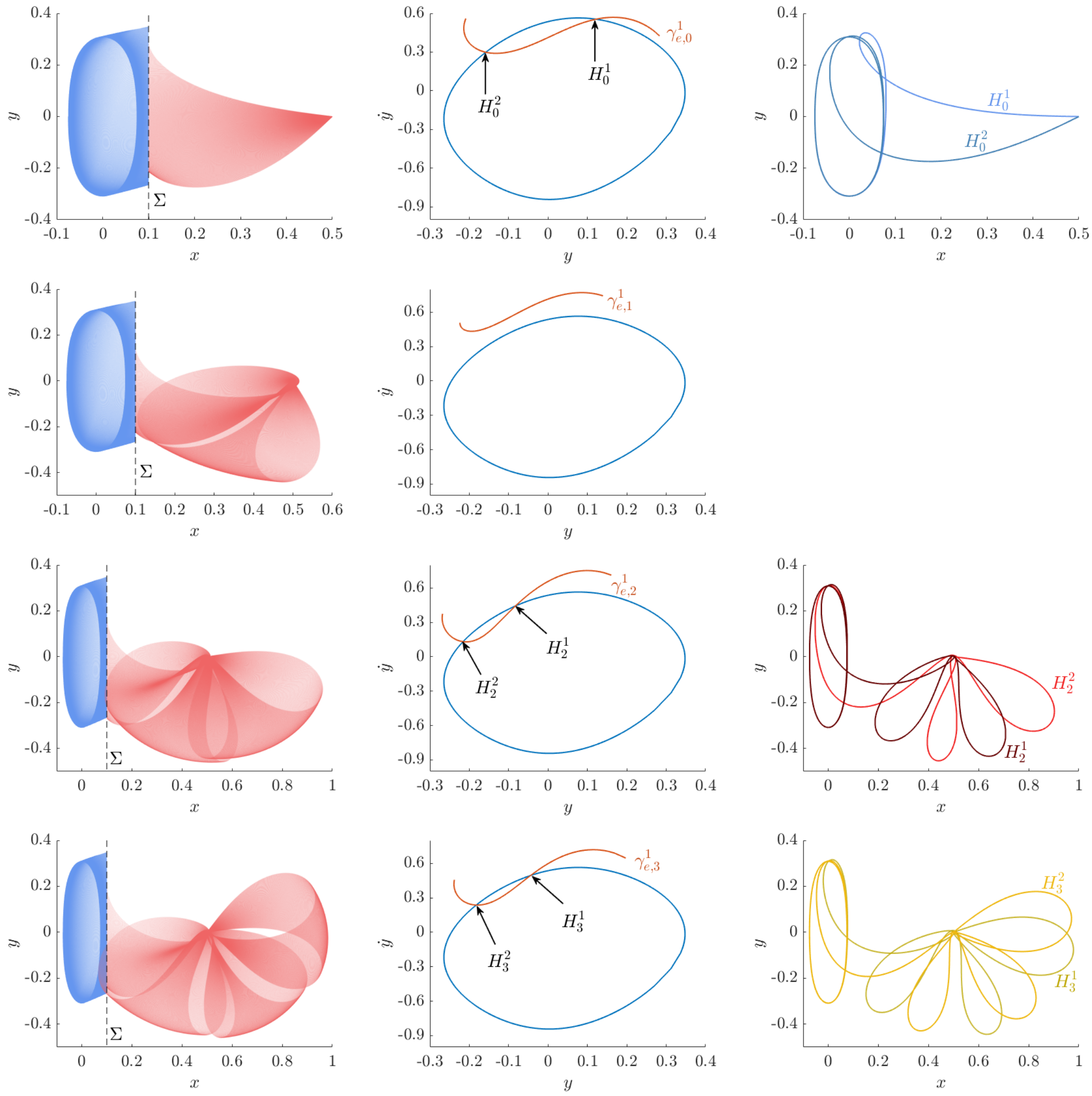

Figure 5: $\mu = 0.5$, $C = C_{L_2}$. Left. (x, y) projection. A set of ejection orbits of $W^e(P_1)$ (in red) such that after n close passages around P_1 reach Σ. ($n = 0$ first row, $n = 1$ second row, $n = 2$ third row, $n = 3$ fourth row). Also the orbits of $W^{s,+}(LPO_1)$ (in blue) up to Σ^+ are plotted. Middle. (y, y') projection of curves $\gamma_s^{+,1}$ (in blue) and $\gamma_{e,n}^1$ (in red). Right. (x, y) projection of two heteroclinic connections, H_n^1 and H_n^2, ejecting from P_1 and tending to the LPO_1. We remark that for $n = 1$ figure right does not appear since there are no heteroclinic orbits in this case as shown on the middle plot.

$W^e(P_1)$ (as explained in Subsection 3.2) up to Σ, giving rise to a curve denoted by γ_e and to look for intersection points between both curves. Each intersection point belongs to a heteroclinic connection, since the solution at this intersection point, integrated forward in time, tends asymptotically to the LPO_1 and backwards in time to the primary P_1.

In order to be more precise, and consider not only the first intersection but the i-th intersection with Σ, to take into account the number n of close passages around the primary, to distinguish between the stable or unstable manifold $W^{s,u}(LPO_1)$ and the branch $+, -$, and the possibility of ejection/collision (we will use a subscript e/c), we now provide the detailed description of the notation we will use at the same time as the steps involved to compute heteroclinic orbits. We remark that all the notation introduced is the necessary one to distinguish among the different properties we want to take into

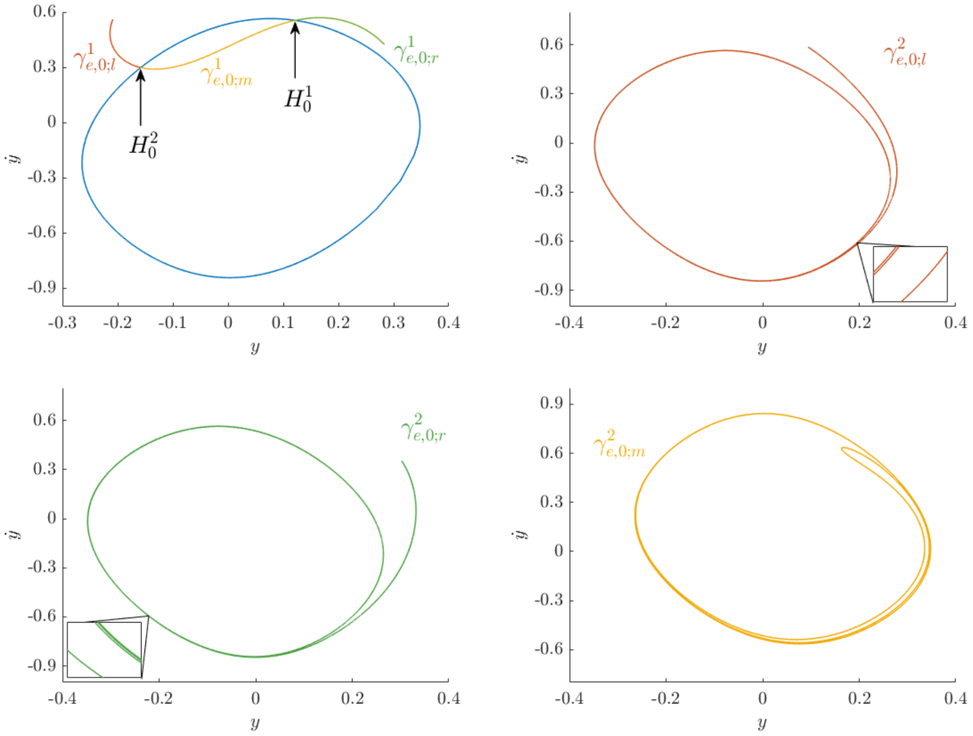

Figure 6: $\mu = 0.5$, $C = C_{L_2}$. $(y, \dot{y})$ projection. Top left. Curve $\gamma_s^{+,1}$ in blue and $\gamma^1_{e,0}$ as the union of the piece $\gamma^1_{e,0;l}$ (in red), $\gamma^1_{e,0;m}$ (in yellow) and $\gamma^1_{e,0;r}$ (in green). The points in $\gamma^1_{e,0;l} \cup \gamma^1_{e,0;r}$ belong to non transit orbits and the points in $\gamma^1_{e,0;m}$ belong to transit ones. The spiralling curves $\gamma^2_{e,0;l/m/r}$ are obtained following the flow, forward in time, of points in $\gamma^1_{e,0;l}$ (top right), $\gamma^1_{e,0;r}$ (bottom left), up to Σ^+; and $\gamma^1_{e,0;m}$ (bottom right), up to Σ^-.

account.

(i) The first step to obtain a heteroclinic orbit from P_1 to the LPO_1 is to compute the corresponding orbit LPO_1 and its 2D positive stable manifold branch ($W^{s,+}(LPO_1)$) backwards in time up to a given Poincaré section Σ^+ defined by $x = x_{L_1} + d$ (for a suitable $d > 0$), giving rise to a $1D$ closed curve $\gamma_s^{+,1}$. In Figure 5 we take $\mu = 0.5$, $C = C_{L_2}$ and $d = 0.1$ so Σ^+ defined by $x = 0.1$; we show $W^{s,+}(LPO_1)$ ((x, y) projection in blue) on the left figures, and the curve $\gamma_s^{+,1}$ ((y, y') projection in blue) on the middle ones. In order to obtain an heteroclinic orbit from the LPO_1 to P_1, we will consider the intersection curve $\gamma_u^{+,1}$ obtained from $W^{u,+}(LPO_1) \cap \Sigma^+$ (integrating forward in time).

Similarly, taking into account the Poincaré section Σ^- defined by $x = x_{L_1} - d$ and the branch $W^{s,-}(LPO_1)$ or $W^{u,-}(LPO_1)$, we obtain the curve $\gamma_s^{-,1}$ from the intersection $W^{s,-}(LPO_1) \cap \Sigma^-$, or the curve $\gamma_u^{-,1}$ from the intersection $W^{u,-}(LPO_1) \cap \Sigma^-$.

We generalise the notation for the curve $\gamma_{u/s}^{\pm,j}$ when considering the j-th crossing of the manifold of the LPO_1 with $\Sigma^\pm$.

So, roughly speaking, we consider the orbits that leave the LPO_1 asymptotically backwards in time up to the Poincaré section, giving rise to one curve.

(ii) The second step is to compute the 2D manifold of the orbits ejecting from (colliding to) the primary P_i, $i = 1$ or 2, $W^{e/c}(P_i)$, describing n *close passages* around the primary P_i (from which the orbit started) and crossing Σ (which will be a chosen Σ^+ or Σ^-). We will denote $\gamma^1_{e,n}$ ($\gamma^1_{c,n}$) the

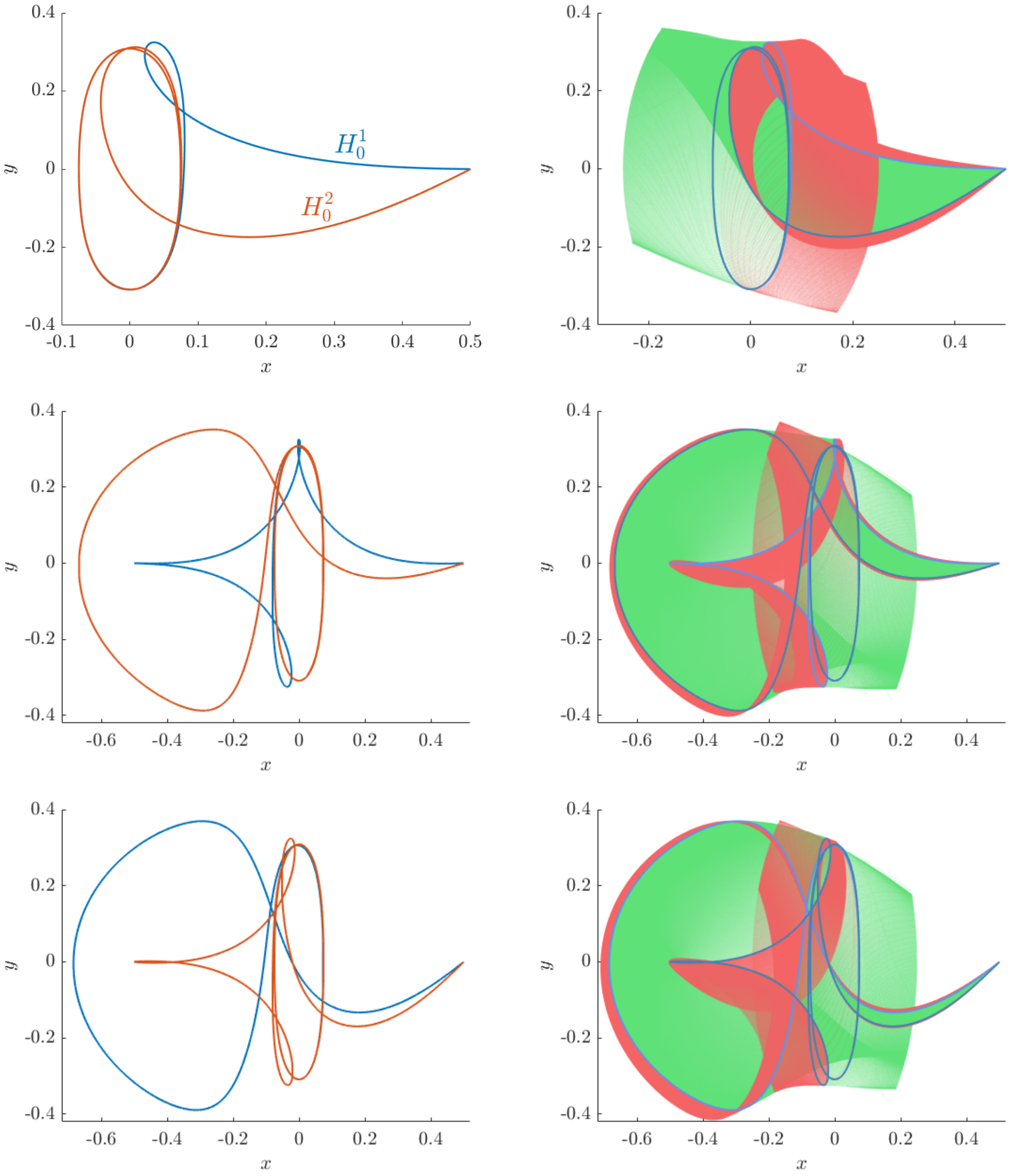

Figure 7: $\mu = 0.5$, $C = C_{L_2}$, (x, y) projection. Top. The two heteroclinic connections $P_1 - LPO_1$, H_0^1 and H_0^2, with $n = 0$ close passages around P_1 with initial angles θ_0^i, $i = 1, 2$ (left). These angles are the end points of the transit interval $I_0 = (\theta_0^1, \theta_0^2)$. Right, orbits that after ejecting from P_1, either transit to the region around P_2 (in green) or do not transit (in red). Transit orbits (in green) follow $W^{u,-}(LPO_1)$; non-transit ones (in red) follow $W^{u,+}(LPO_1)$. Middle and bottom. Left. Two new heteroclinic orbits with angles θ_0 close to θ_0^1 (middle), and close to θ_0^2 (bottom). Right. In green orbits ejecting from P_1, pass close to the LPO_1, transit to the region around P_2, pass near the LPO_1 and either transit to the region around P_1 (in green) or bounce back to the region around P_2 (in red).

corresponding curve if the ejecting (colliding) body is P_1 and $\bar{\gamma}_{e,n}^1$ ($\bar{\gamma}_{c,n}^1$) if the ejecting (colliding) body is P_2. Due to the restriction of the n close passages around the primary for fixed n, only a piece of curve, not a closed one, for $\gamma_{e/c,n}^1$ or $\bar{\gamma}_{e/c,n}^1$ is obtained. We plot the (y, y') projection of the curves $\gamma_{e,n}^1$, for $n = 0, 1, 2, 3$ in Figure 5 middle, for $\mu = 0.5$, $C = C_{L_2}$.

We generalise the notation for the curve $\gamma_{e/c,n}^j$ (or $\bar{\gamma}_{e/c,n}^j$) when considering the 2D manifold of orbits

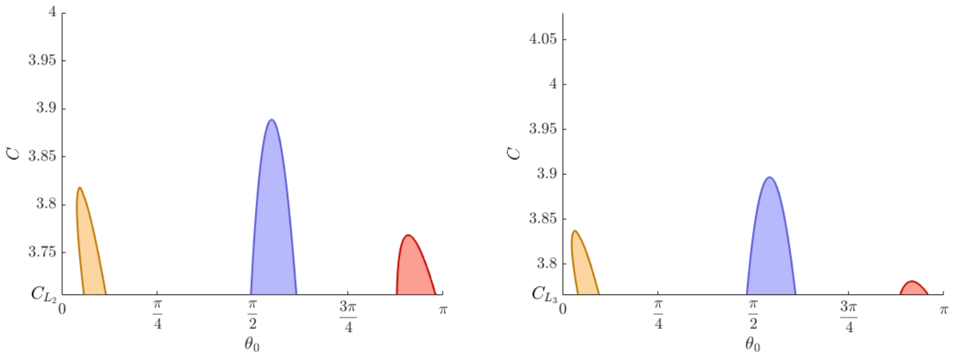

Figure 8: $\mu = 0.5$ and $\mu = 0.7$, primary transition intervals when varying C. The corresponding transition regions are in blue for $n = 0$, in red for $n = 2$, and in brown for $n = 3$. For each value of C given, an interval of ejection orbits (each one identified by its value θ_0) which are transit orbits is obtained. The interval depends on the value of n.

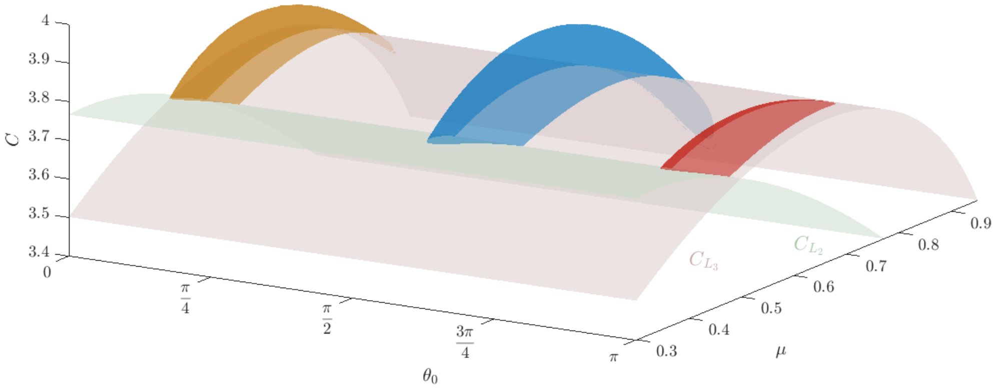

Figure 9: 3D plot of heteroclinic connections between the primary of mass μ and the LPO_1 when varying $\mu \in (0, 1)$, $C \in [C_{L_{2,3}}, C_{L_1})$, taking $n = 0, 2, 3$. The corresponding transition regions are in blue for $n = 0$, in red for $n = 2$, and in brown for $n = 3$. This figure is the generalization of Figure 8 varying μ.

that eject/collide with a primary, describe n close passages around it and cross Σ at the j-th time.

So, roughly speaking, we consider the orbits that eject from the primary, forward in time, describe n close passages to that primary and reach the Poincaré section, giving rise to another curve.

(iii) Last step is to compute the intersection points between both curves obtained in (i) and (ii). In order to fix ideas, let us consider heteroclinic orbits $P_1 - LPO_1$. Each intersection point belonging to $\gamma_s^{+,1} \cap \gamma_{e,n}^1$ gives rise to a heteroclinic connection between P_1 (integrating backward in time) and the LPO_1 (integrating forward in time). We will label such heteroclinic connection by H_n (and abusing notation, also the intersection points will be labelled the same way). We point out that for $n = 0, 2, 3$, there exist typically two heteroclinic connections, labelled by H_n^1 and H_n^2, and there are no heteroclinic connections for $n = 1$. See Figure 5 middle and also both heteroclinic orbits (the (x, y) projection) in the right plots (for $n = 0, 2, 3$ at the first, third and fourth rows respectively).

The location of these heteroclinic connections is relevant for our purpose of determining transit regions. We have just shown that fixed n, we obtain points H_n^1 and H_n^2. So there is a set of points (located on the red curve $\gamma_s^{+,1}$) of Figure 5 middle –first, third and fourth rows–) between H_n^1 and H_n^2. Such points belong to ejection orbits, each one characterized by a value of θ_0 as already described in subsection 3.2. Moreover such points are located inside the blue curve in Figure 5 middle). This means that any such point comes (backwards in time) from ejection and goes (forward in time) to the region around P_2, that is each such point belongs to a transit orbit. So regarding the set of initial angles of these transit orbits, we have an interval that we denote by $I_n = (\theta_n^1, \theta_n^2)$, called *transit interval* such that for any $\theta_0 \in I_n$, the associated ejecting orbit, with initial angle θ_0, is a transit orbit, since it will be inside $W^{s,+}(LPO_1)$ (i. e. the intersecting point of the orbit with Σ_+ will be a point on $\gamma_s^{+,1}$ –the red curve– inside $\gamma_s^{+,1}$ –the blue one–). More specifically, the particle will be ejected from the primary P_1, will describe a trajectory such that will have n close passages around the primary P_1, afterwards will cross Σ and will visit the region around the other primary P_2. The set of points in the curve $\gamma_{e,n}^1$ belonging to transit orbits will be denoted by $\gamma_{e,n;m}^1$ (m stands for middle). See Figure 5 and Figure 6 top left. We show the set of transit orbits in green Figure 7 top for $n = 0$ right. We neatly see the two heteroclinic orbits (in red and blue on the left plot) H_0^1, H_0^2 and the whole set of transit orbits in between on the right plot. An interesting remark here that will be relevant later on is that all such orbits are transit orbits, but notice that the closer θ_0 is to θ_n^i, $i = 1, 2$, the closer the ejecting trajectory passes near the LPO_1 describing some rounds around it before transiting to the region around P_2.

Interestingly, while the piece $\gamma_{e,n;m}^1$ contains points belonging to transit orbits, we wonder what happens with the remaining part of the curve $\gamma_{e,0}^1 - \gamma_{e,0;m}^1$ in Figure 6 top left. As foreseen, since such points are outside the curve $\gamma_s^{+,1}$ (the blue one on the top left figure), they belong to non transit orbits. Let us label the two pieces as $\gamma_{e,n;l}^1$ and $\gamma_{e,n;r}^1$ (l and r stand for left and right respectively). See Figure 6 top left for $n = 0$. For any point in $\gamma_{e,0;l}^1 \cup \gamma_{e,0;r}^1$, the corresponding orbit, that is outside $W^{s,+}(LPO_1)$, will be a non transit orbit with the initial θ_0 outside I_n (but close to it): the particle, after ejecting from P_1, having n close passages around P_1 and going close to Σ, will return to the same region around P_1 (where it came from). We plot in Figure 7 top right the set of ejection orbits from P_1 that become non-transit orbits and *bounce back* to the region around P_1, in red.

In summary, we have $\gamma_{e,n}^1 = \gamma_{e,n;l}^1 \cup \gamma_{e,n;m}^1 \cup \gamma_{e,n;r}^1$. A point in $\gamma_{e,n;l}^1 \cup \gamma_{e,n;r}^1$ belongs to an ejecting orbit which is a non-transit orbit, whereas a point in $\gamma_{e,n;m}^1$ belongs to a transit one; and the end points of $\gamma_{e,n;m}^1$ belong to heteroclinic connections acting as barrier between the two kinds of motions.

The discussion about the role of the transition interval to distinguish between transit and non transit ejection orbits is based on the existence of such transition interval I_n. However the existence of the transition interval I_n depends on n, μ and C, that is, for n given, the presence of heteroclinic connections $P_i - LPO_1$ is not guaranteed for all μ and $C \geq C_{L_{2,3}}$. We show in Figure 8, the transition intervals for $\mu = 0.5$ and $\mu = 0.7$ for $C \geq C_{L_{2,3}}$ (in blue for $n = 0$, in red for $n = 2$ and in brown for $n = 3$). We can see, that fixed μ and n, for each suitable value of C (on the y axis) there is an interval I_n of initial angles θ_0 (on the x axis) of ejecting-transit orbits and the points on the boundary of the transition interval correspond to the two specific values of θ_0 of heteroclinic connections $P_1 - LPO_1$. However, there is a maximum value of C where the two curves $\gamma_s^{+,1}$ and $\gamma_{e,n}^1$ become tangent and there is a single heteroclinic connection $P_1 - LPO_1$. For higher values of C there are no heteroclinic connections.

So far we have shown the heteroclinic connections $P_1 - LPO_1$ with $n = 0, 2, 3$ close passages around P_1 as well as the transition interval I_n, just for single values of μ ($\mu = 0.5$ and 0.7). We have done massive computations in order to obtain the transition interval for any value of $\mu \in (0, 1)$, any value of $C \in [C_{L_{2,3}}, C_{L_1})$ (recall the location of L_i, $i = 1, 2, 3$ for any μ), and for $n = 0, 1, 2, 3$. See Figure 9. The blue, red and brown surfaces provide the transition intervals (θ_0 values on the x axis) respectively for any μ on the y axis, and a suitable range of values of C on the z axis. Several comments must be done concerning this figure: (i) We remark that for $n = 1$, neither varying $C \in [C_{L_{2,3}}, C_{L_1})$ nor $\mu \in (0, 1)$, we have not found any heteroclinic connection ejecting from P_i ($i = 1$ or 2), describing

1 close passage around P_i and tending asymptotically to the LPO_1. (ii) Heteroclinic connections $P_i - LPO_1$ do not exist for all μ and $C \geq C_{L_{2,3}}$. For n given, there exist minimum and maximum values of μ for which the heteroclinic connections exist. These extrema values correspond to tangencies between the curves $\gamma_s^{+,1}$ and $\gamma_{e,n}^1$. Just before (after) the tangency, the curves $\gamma_s^{+,1}$ and $\gamma_{e,n}^1$ do not intersect (intersect) in two points, which provide the transition interval (any slice in Figure 9 with μ fixed). (iii) Another important remark is that, given μ, such heteroclinic connections only exist for values of C in a suitable interval for $C \geq C_{L_{2,3}}$ and such interval depends on μ. We showed the particular cases $\mu = 0.5$ and $\mu = 0.7$ in Figure 8.

So, from the previous exploration we conclude that the two heteroclinic connections H_n^1 and H_n^2 (given n) –or equivalently the transition interval $I_n = (\theta_n^1, \theta_n^2)$– determine a barrier that allows to distinguish between ejection orbits that (after describing n close passages to the primary) are transit orbits or non transit. That is we have a *first* classification on the dynamical behaviour of the ejection orbits regarding its transit/non transit character. This is the simple part of the story we have seen so far. The story line goes on when we ask ourselves what happens if there are other heteroclinic connections $P_i - LPO_1$. The answer is that we can use *other* heteroclinic connections, in general, to know which region (around the big primary or around the small one) the ejection orbit will visit along its trajectory, and therefore such heteroclinic connections will provide an additional way to classify the dynamical behaviour of the ejection orbits.

So, next, in this Section we just want to discuss an example of the consequences of the appearance of two heteroclinic orbits *close* to the heteroclinic connection H_0^1 (and similarly the appearance of two heteroclinic orbits *close* to the heteroclinic connection H_0^2). In the next Section, a deeper analysis is carried out when there appear not two but infinitely many heteroclinic orbits. So it is worthwhile understanding, first, what happens in this simple situation.

Let us describe the plots in Figure 7 (all the plots contain the the projection in (x, y) variables). As mentioned, we show on the top left figure, the two heteroclinic connections H_0^i, $i = 1, 2$, with initial angles $\theta_0^1 = 1.5586742225724$ and $\theta_0^2 = 1.932752613334$ respectively and in the top right figure the set of ejection and transit orbits (in green) and two sets of ejection and non-transit orbits (in red). As previously discussed, the two heteroclinic connections provide the barriers between transit and non-transit orbits. Now we consider two new heteroclinic orbits $P_1 - LPO_1$, with initial θ_0 close to θ_0^1; more specifically, we denote the new values by $\theta_0^{1,1} = 1.584919597063$ and $\theta_0^{1,2}$ (the superscripts being $1, 1$ and $1, 2$ because they are close to $\theta_0^1 = 1.702359169703$). Notice that $(\theta_0^{1,1}, \theta_0^{1,2}) \subset (\theta_0^1, \theta_0^2)$.

The first remark is that we can clearly see that the two new heteroclinic connections behave differently from H_0^1 in the sense that after ejecting from P_1, do visit a region around P_2 and end asymptotically in the LPO_1 (see Figure 7 middle) whereas H_0^1 does not visit any region around P_2. The key point is that such two heteroclinic connections provide new barriers of transit and non transit, and therefore determine an additional *second* classification of the ejecting orbits in the previous bigger set of ejecting orbits in the top figure. More precisely, for the set of ejection orbits with $\theta_0 \in (\theta_0^1, \theta_0^2)$ we can distinguish two kinds of behaviour: first, the ejection orbits in the thinner set determined by the two new heteroclinic orbits (that is, whose $\theta_0 \in (\theta_0^{1,1}, \theta_0^{1,2})$); they eject from P_1, transit to the region around P_2 (since $\theta_0 \in (\theta_0^1, \theta_0^2)$, i. e. first classification), and transit again towards the region around P_1 (since $\theta_0 \in (\theta_0^{1,1}, \theta_0^{1,2})$, i. e. second classification). See the green set of orbits in Figure 7, middle right. Second, the ejection orbits with $\theta_0 \in (\theta_0^1, \theta_0^2)$ but outside the thinner set (that is, whose $\theta_0 \notin (\theta_0^{1,1}, \theta_0^{1,2})$). Such orbits eject from P_1, transit to the region around P_2 (since $\theta_0 \in (\theta_0^1, \theta_0^2)$, i. e. first classification) but are non transit orbits and bounce back and remain on the same region around P_2 (second classification). See the red set of orbits in Figure 7, middle right.

A similar behaviour concerning transit/non transit (first classification) and transit/non transit (second classification) can be described for the two new heteroclinic orbits, with initial $\theta_0^{2,1} = 1.867534417000$, $\theta_0^{2,2} = 1.925408730327$, respectively close to θ_0^2, that can be seen in the bottom Figure 7. Notice that $(\theta_0^{2,1}, \theta_0^{2,2}) \subset (\theta_0^1, \theta_0^2)$.

So far, we have discussed the dynamical behaviour of the ejection orbits, transit/non transit, taking into account the effect of the LPO_1 and the heteroclinic connections $P_1 - LPO_1$. Now, we may add a new ingredient to be even more precise in the the classification of the ejection orbits, taking into account the number of turns that the ejection orbit (whether it is transit or non transit) describes around the LPO_1, when it passes close to it. To clarify this idea, let us consider first the points on $\gamma^1_{e,n;l}$ and $\gamma^1_{e,n;r}$ (that belong to non-transit orbits) and for each such point we follow the corresponding trajectory (that started ejecting from P_1) by the flow up to the Poincaré section Σ^+. In a natural way we denote the corresponding curves by $\gamma^2_{e,n;l}$ and $\gamma^2_{e,n;r}$. Since the points on $\gamma^1_{e,n;i}$, $i = r, l$ are very close to a point that belongs to a heteroclinic orbit $P_1 - LPO_1$, the resulting orbits are very close to the manifold branch $W^{u,+}(LPO_1)$, so such orbits describe a trajectory that surrounds the LPO_1 several times and follow the manifold $W^{u,+}(LPO_1)$; therefore the resulting curves, $\gamma^2_{e,n;l}$ and $\gamma^2_{e,n;r}$, spiral on and on towards the curve $\gamma^{+,1}_u$. More precisely, the set of points of every spiral turn of the curve $\gamma^2_{e,n;l/r}$ correspond to points that, on the section Σ, track the whole LPO_1 (sort to speak). So the infinitely many spiral turns of the curve $\gamma^2_{e,n;l/r}$ are intrinsically related to the number k of turns (k from 0 to infinity) that the ejection orbit does around the LPO_1. We plot in Figure 6 the resulting spiralling curves for $\mu = 0.5$, $C = C_{L_2}$ and $n = 0$.

Second we reason analogously with the points in the curve $\gamma^1_{e,n;m}$. Since they belong to ejecting transit orbits, we follow the curve by the flow up to Σ^- (instead of Σ^+) giving rise to a double spiral, $\gamma^2_{e,n;m}$ that spirals on and on towards the curve $\gamma^{-,1}_u$. See Figure 6 right. In the three plots the spiral curves look fastly 'glued' (although always infinitely spiralling) to the corresponding curve $\gamma^{\pm,1}_u$.

In accordance with the aforementioned considerations, the natural code we are going to use in order to classify an ejecting orbit will be the following:

$$E^n_i - PO^k - P^j_l - ...$$

which stands for: an ejecting orbit from the primary P_i ($i = 1$ or 2), describes n close passages around this primary before going close to the LPO_1, surrounds k times the LPO_1, and visits the region around P_l ($l = 1$ or 2), describing j close passages around this primary,... Therefore, this code determines the geometrical trajectory the ejection orbit is actually doing. See Figure 10 for two particular examples of ejection orbits. It is clear that symbolic dynamics might be introduced.

In the particular case that the orbit is an EC orbit, the code will be

$$E^n_i - PO^k - C^j_l$$

where now C^j_l means that, after j close passages around the primary P_l, the particle ends at collision with it.

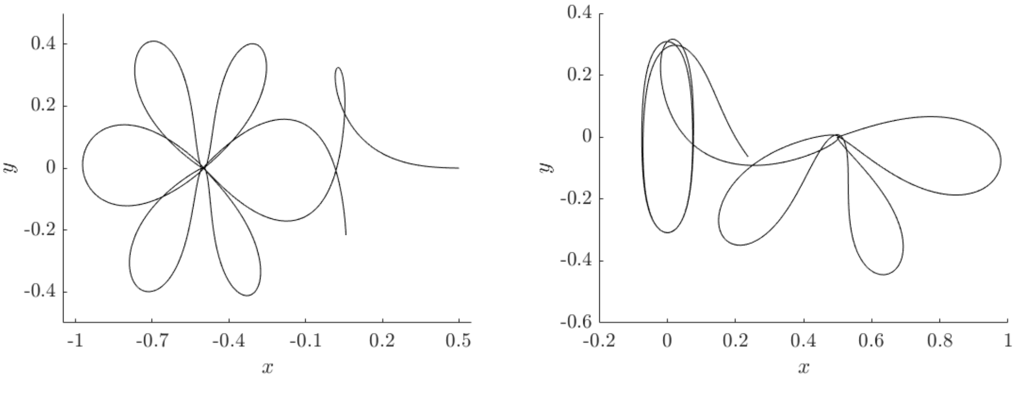

Figure 10: $\mu = 0.5$, $C = C_{L_2}$. (x, y) projection. Ejection orbit $E^0_1 - PO^0 - P^6_2 - ....$ (left) and $E^3_1 - PO^2 - ....$ (right).

Just summarizing, so far we have described the role of the two simple heteroclinic connections $P_1 - LPO_1$ (providing a first classification), given by θ_0^1, θ_0^2 and the couple of new heteroclinic connections $\theta_0^{1,1}$, $\theta_0^{1,2}$ and $\theta_0^{2,1}$, $\theta_0^{2,2}$ (providing an additional second classification). We know that the two simple heteroclinic connections come from the requirement that the ejection orbit has $n = 0$ close passages to P_1 and reaches the Poincaré section Σ matching with a point belonging to $W^{s,+}(LPO_1)$. But at this point we would like to know where the other new heteroclinic orbits come from. The answer involves the existence of homoclinic orbits to the LPO_1, that is orbits that asymptotically tend to the LPO_1 forward and backward in time.

Actually the situation is much more involved, because there appear infinitely many homoclinic orbits and as a consequence infinitely many heteroclinic connections $P_1 - LPO_1$, giving rise to a chaotic behaviour. Thus, once we have described the simple, or *regular* situation in this Section, let us analyse the effects of the existence of infinitely many homoclinic and heteroclinic connections. This is one purpose of the next Section.

5 Regular motion vs chaos. The role of the LPO_1

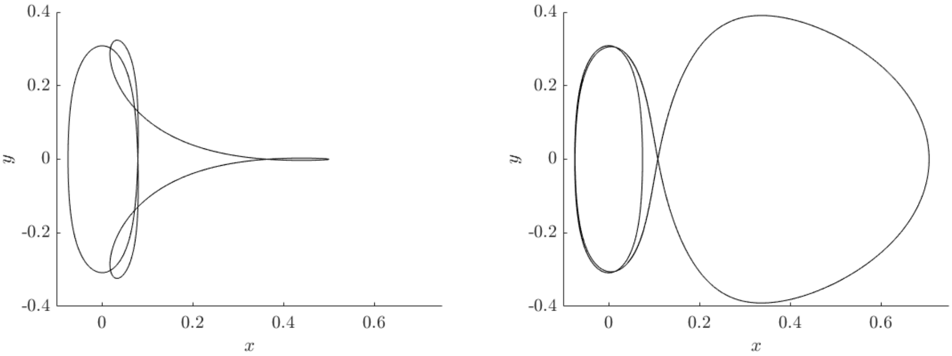

Figure 11: $\mu = 0.5$, $C = C_{L_2}$. Two different homoclinic orbits to the LPO_1, HO^1 (left) and HO^2 (right). (x, y) projection.

In the previous Section we have described a *regular* kind of motion in the sense that the transition interval provides a barrier to distinguish between transit and non transit ejection orbits, which becomes a *first* classification for the ejection orbits. That is the dynamical behaviour of the ejection orbits is related to the heteroclinic connections. However, we have also described an example to show that the appearance of two new heteroclinic orbits close to H_0^1 (or H_0^2) provide an additional *second* classification of the ejection orbits: the orbits eject from the primary, are transit orbits (first classification), and once they are on the region around the other primary, they can be classified as transit or non transit orbits (second classification). One purpose of this Section is to show that, actually, there are infinitely many heteroclinic connections between the primary and the LPO_1. This infinity is related to the existence of homoclinic orbits to the LPO_1 so this orbit plays a key role here. Moreover the heteroclinic connections are very close to each other. Thus, an immediate consequence is that if we take all of them into account, we have infinitely many ways of classifying an ejection orbit, which results in a chaotic classification.

A second and interesting purpose of this Section is focussed on another chaotic infinity, now related to the EC orbits. We will discuss the mechanism to generate infinitely new EC orbits taking into account the presence of LPO_1.

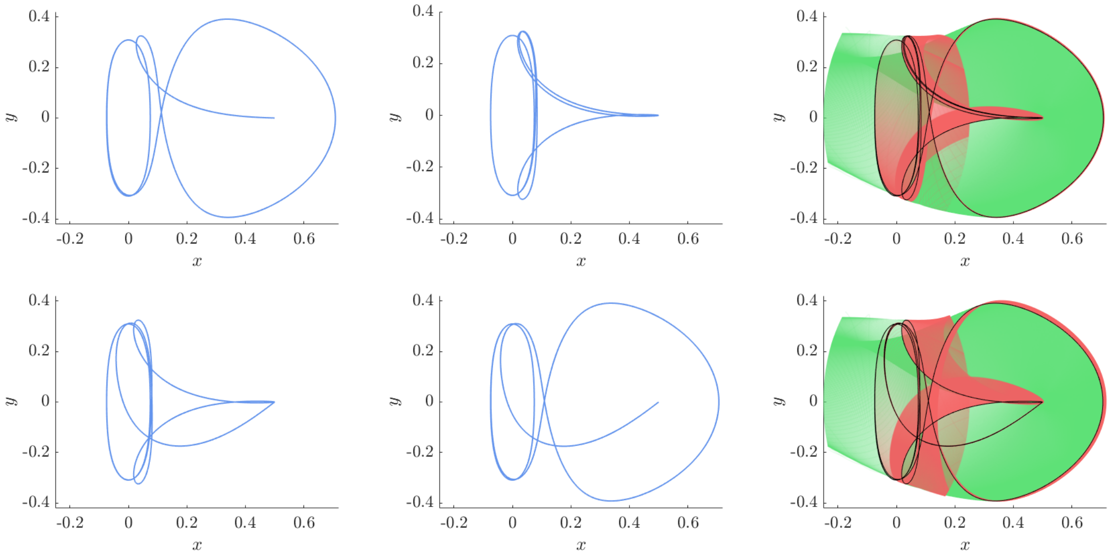

Figure 12: $\mu = 0.5$, $C = C_{L_2}$, (x, y) projection. Left and middle. Two heteroclinic orbits with values of θ_0 equal to $\tilde{\theta}_0^{i,1}$ and $\tilde{\theta}_0^{i,2}$ near near θ_0^i ($i = 1$ in top figure, $i = 2$ in bottom figure). Right. The set of transit orbits (in green) and non-transit ones (in red) are shown.

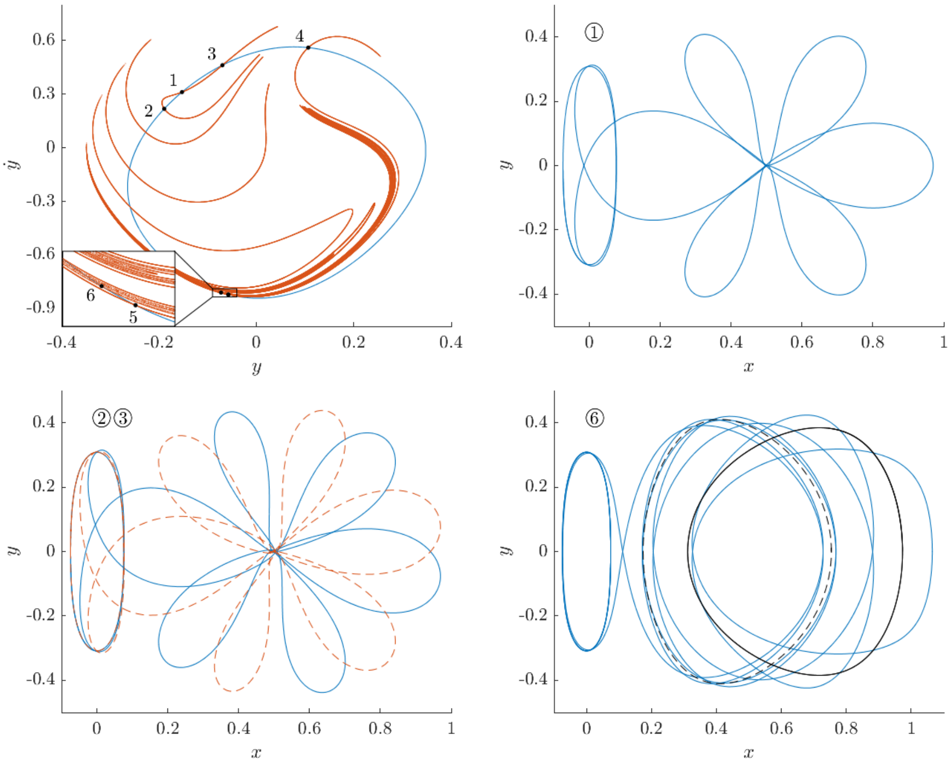

Figure 13: $\mu = 0.5$, $C = C_{L_2}$. Top left. $(y, \dot{y})$ projection. Intersection curve $W^{s,+}(LPO_1) \cap \Sigma^+$ at the first crossing (in blue) and the intersection $W^{u,+}(LPO_1) \cap \Sigma^+$ at the second crossing (in red). Examples of homoclinic orbits: the ones labelled by 1,2,3 and 6. 4 and 5 are shown in Figure 11. The homoclinic orbit 6 involves two periodic orbits, one stable (discontinuous black line) and one unstable (continuous black line).

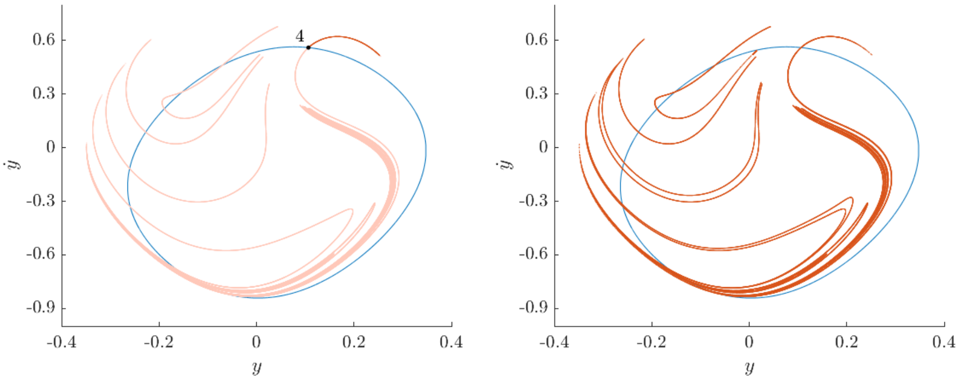

Figure 14: $\mu = 0.5$, $C = C_{L_2}$. $(y, \dot{y})$ projection. Left. Curves $\gamma_u^{+,2}$ and $\gamma_s^{+,1}$. Right. From curve $\gamma_u^{+,2}$, we take the *small darker red piece* external to $\gamma_s^{+,1}$ (the blue one) and ending at point 4. The fourth crossing of such small piece with Σ^+ gives rise to the infinite foliation of replications of the second crossing curve $\gamma_u^{+,2}$ shown on the plot.

5.1 Infinitely many heteroclinic orbits $P_i - LPO_1$

In the previous Section we have shown *big* transition intervals of values of θ_0, that is big sets of ejection orbits that can be classified as transit or non-transit when they pass close to the LPO_1. We have also remarked that the barriers of such intervals are the heteroclinic orbits $P_i - LPO_1$.

However, the determination of such transition intervals, whose end points are initial angles for heteroclinic connections $P_i - LPO_1$, is not that simple: we will show that there are infinitely many heteroclinic connections $P_i - LPO_1$. A crucial point to understand where this infinity comes from is the existence of homoclinic orbits of the LPO_1.

Let us discuss this complexity just taking into account two homoclinic orbits (later on we will consider infinitely many homoclinic orbits). The simulations are done for $\mu = 0.5$ and $C = C_{L_2}$.

Let us start with two simple homoclinic orbits of the LPO_1, shown in Figure 11, and called HO^1 (on the left) and HO^2 (on the right). Roughly speaking the shape of HO^1 ((x, y) projection) is composed of a curved triangular shape plus the asymptotic shape to the LPO_1, whereas HO^2 ((x, y) projection) is composed of a big loop (close to circular) shape plus the asymptotic shape to the LPO_1.

A main consequence of such homoclinic orbits is that there exist infinitely many heteroclinic connections $P_1 - LPO_1$ with an initial angle θ_0 *very close* to θ_0^1 such that the associated heteroclinic connections $P_1 - LPO_1$ are rather different. More precisely, let us describe how these infinitely many appear. First, look just at three (not infinite but just three) simple heteroclinic connections which have a *quite similar path from ejection to (near) the* LPO_1 (the piece of trajectory from ejection up to the first small loop of the three orbits are almost the same), that is with values of θ_0 very close to each other: the first one, H_0^1 (in Figure 7 top left), just ends asymptotically at the LPO_1. The second one with $\theta_0 = \tilde{\theta}_0^{1,1} = 1.553258226788$ (in Figure 12 top left), when the particle is near the LPO_1, does not surround the LPO_1 but follows the path of the big loop of the homoclinic orbit HO^2 once and ends asymptotically at the LPO_1. The third heteroclinic orbit with $\theta_0 = \tilde{\theta}_0^{1,2} = 1.557995153267$ does not surround the LPO_1 but follows the path of the curved triangular piece of the homoclinic orbit HO^1 and ends asymptotically at the LPO_1. See Figure 12 top middle. Notice that all of them describe 0 turns along the first piece of trajectory (from ejection up to the first small loop). We call them three basic heteroclinic connections.

Therefore, we have the same phenomenon described in the Figure 7 as far as the classification of the trajectory of ejection orbits is concerned, we obtain a very thin interval of values of θ_0 near θ_0^1 that separates transit of non-transit orbits. This is shown in Figure 12 top right. However now the range of the transition interval $(\tilde{\theta}_0^{1,1}, \tilde{\theta}_0^{1,2})$ is remarkably thinner.

We have a similar situation when we consider the homoclinic orbits HO^i, $i = 1, 2$ and the heteroclinic connection H_0^2. There are two heteroclinic connections with $\theta_0 = \tilde{\theta}_0^{2,1} = 1.932919335638$ and $\theta_0 = \tilde{\theta}_0^{2,2} = 1.934043834973$, respectively, values very close to θ_0^2. The three of them describe (almost) the same path from ejection up to the first big loop (see Figure 7 top left and Figure 12), however afterwards one goes directly to the LPO_1, another one describes a path close to the curved triangular piece before ending to the LPO_1 (see Figure 12 bottom left) and the other one describes a piece of the big circular loop before ending to the LPO_1 (see Figure 12 bottom middle). Notice that all of them describe 0 turns along the first piece of trajectory (from ejection up to the first big loop). We call them three basic heteroclinic connections (one of them does not involve a homoclinic orbit, and two of them do involve either one or the other homoclinic orbit). Again a remarkably thin transition interval appears very close to θ_0^2.

So far we have shown the two simplest (or basic) heteroclinic connections involving HO^1, with an initial $\tilde{\theta}_0^{1,1}$ and $\tilde{\theta}_0^{1,2}$ (respectively) quite close to each other and near θ_0^1. And similarly for $\tilde{\theta}_0^{2,1}$ and $\tilde{\theta}_0^{2,2}$ involving HO^2.

But this is the *simple version* of the description of heteroclinic connections involving the homoclinic orbits HO^1 and HO^2. From the above discussion we want to emphasize that we have considered six heteroclinic connections, all of them sharing a common property: each one describes its own path but all of them describe zero turns before ending asymptotically to the LPO_1. We will say that the number of turns is $k = 0$.

We mentioned above that the situation is much more complex. Actually there are infinitely many heteroclinic connections $P_1 - LPO_1$. Let us explain how they appear.

A first mechanism is the following. We can obtain new heteroclinic connections $P_1 - LPO_1$ just with the same kind of trajectory as the four heteroclinic orbits described in Figure 12 top and bottom, left and middle, but with one difference: the first piece is the same as before, now the trajectory describes k turns around the LPO_1, and afterwards describes the *same* path (of course almost the same) as the previous ones. So we have four new heteroclinic orbits for $k = 1$, four new ones for $k = 2$,...., four new ones for each number of k turns given. In that way, we obtain infinitely many heteroclinic orbits. Or equivalently, we have shown three plus three heteroclinic connections, with $k = 0$, the basic ones. For any k, we have a new triplet of heteroclinic connections which share (almost) the same first piece of trajectory (from ejection to the first loop), then describe k turns to the LPO_1 and then each one follows (almost) the same path as each of the three basic heteroclinic connections. In Figure 12, we have just considered the simplest ones ($k = 0$).

The second mechanism is a generalization of the previous one. Of course, there are other infinitely many families of heteroclinic orbits, not only playing with the number k of turns around the LPO_1, but also playing with two homoclinic orbits. More specifically, above we have considered two ternaries of heteroclinic connection: for the first triplet, one does not involve any homoclinic orbit, the second one involves one homoclinic orbit and the third one involves another (different) homoclinic orbit. And similarly for the second triplet. Let us describe, for example a new heteroclinic connection: we take the heteroclinic connection in Figure 12 top left. We might construct a new heteroclinic connection (with θ_0 extremely close to $\tilde{\theta}_0^{1,1}$) as follows: the first piece from ejection to the first small loop (almost) the same, then k turns around the LPO_1, then the path of the big circular loop (of HO^2), then m turns around the LPO_1, then the path of the curved triangle, then tending asymptotically to the LPO_1. Another different one would be (almost) the same but before ending to the LPO_1, the trajectory might follow the curved triangle piece, the j turns around the LPO_1, then follow the big circular loop, then l turns around the LPO_1, then ..., before ending to the LPO_1, where the dots ... stand for any pre-desired combination of turns around the LPO_1, the big circular loop and/or the curved triangle.

So, in conclusion, for values of θ_0 extremely close to θ_0^1 or θ_0^2, a chaotic behaviour, that is infinitely many heteroclinic connections $P_1 - LPO_1$, show up.

But the complexity procedure does not end here. Why? Because there are, not only two (HO^1 and HO^2), but infinitely many homoclinic orbits of the LPO_1 involving other invariant objects. So we may apply the previous mechanisms playing with any (one or more) of this infinity of homoclinic orbits to obtain a new *chaotic* infinity of heteroclinic connections $P_1 - LPO_1$.

So now, quite naturally, we want to talk about the homoclinic orbits to the LPO_1, how to compute them and how many of them the RTBP has in the range of C considered.

First, let us show a systematic way to find the infinity of homoclinic orbits to the LPO_1. Just consider the first crossing of $W^{s,+}(LPO_1)$ with Σ^+, that is $\gamma_s^{+,1}$ which is a nice S^1 shaped curve (see Figure 13 top left in blue), and the second crossing of $W^{u,+}(LPO_1)$ with Σ^+, $\gamma_u^{+,2}$ which is now a very intricated set of curves (see Figure 13 top in red). Each intersection point between both curves corresponds to a homoclinic orbit of the LPO_1. We can see that there are 'clean' intersections but also 'tongues' concentrated in some area. We have labelled $1, 2, 3, 4$ four clean points and 5 (a not so clean point). See Figure 13 top left. The corresponding homoclinic orbits are shown as follows: 1 in the top right figure, 2 and 3 in the bottom left figure, and 4, 5 are the ones shown in Figure 11. As we can see the role of the path close to collision with the primary P_1 is essential here. But not only the collision plays a role; there are other simple periodic orbits (apart from the LPO_1) that are also involved and that is a reason for the infinity of homoclinic orbits. Just to show an example, we have chosen point 6 in the top left figure which has an associated homoclinic orbit shown in the same figure, bottom right. We have also plotted two periodic orbits involved in the shape of the homoclinic orbit. One periodic orbit is stable (in discontinuous black line) and another one is unstable (in continuous black line). It is clear that the homoclinic orbits is sensitive to the effect of both periodic orbits; in particular the particle surrounds the stable one several times and follows its trajectory to visit the unstable one, then surrounds again the stable one and finally goes towards the LPO_1. In general there are infinitely many periodic orbits which can be stable or unstable, each one potentially playing a role in the homoclinic orbits. The deep analysis of such role is left for a future paper.

Second, we want to emphasize that we can obtain other infinite family of homoclinic orbits of the LPO_1 just taking into account not only the intersection of $W^{u,+}(LPO_1)$ with Σ^+ at the *second* crossing, curve $\gamma_u^{+,2}$, but also the $2k$*-th* crossing, curve $\gamma_u^{+,2k}$. In order to illustrate the richness of this curve, we consider the curve $\gamma_u^{+,2}$ (see Figure 14) and we just take the *small* (darker red) piece of curve ending at point 4 and external to $\gamma_s^{+,1}$ (the blue one). Let us denote it by $\bar{C}$. We follow the flow of such points, integrating forward in time, up to the fourth crossing with Σ^+ (that is we take a suitable small range of values of θ_0 for ejection orbits, such that at the second crossing with Σ^+ they define the points on the small piece of curve $\bar{C}$, and follow these orbits up to the fourth crossing with Σ^+. Actually if we took a very small sub-piece of such curve $\bar{C}$, we would obtain a replication of the Figure 14 left: the closer the sub-piece of curve is to the intersection point (between the blue curve $\gamma_s^{+,1}$ and $\gamma_u^{+,2}$), the similar replication to the Figure 14 left will be obtained. Since the corresponding orbits pass very close to the LPO_1, turning k times the LPO_1, the trajectories from the second to the fourth crossing with Σ^+ will be (almost) a replication of those going from $W^u(LPO_1)$ to the second crossing with Σ^+. Therefore varying k (that is, taking smaller and smaller sub-pieces of the small piece $\bar{C}$) we obtain a foliation of (almost) replications of the curve $\gamma_u^{+,2}$. This foliation is shown in Figure 14 right. Due to the closely packed foliation, the plot apparently looks like the left one but it is not exactly equal.

So we conclude that the structure of homoclinic orbits is amazingly rich.

5.2 Generation of infinitely many EC orbits

This subsection is focussed on describing a mechanism that explains how a chaotic infinity of EC orbits are obtained taking into account the role of the LPO_1. We will distinguish two cases: EC orbits to the same primary and ejection orbits from one primary and collision with the other one.

5.2.1 EC orbits from/to P_1 involving the LPO_1

An EC orbit is a trajectory that belongs to $W^e(P_1) \cap W^c(P_1)$ (recall the notation introduced in Subsection 3.2). So actually we just need to compute such intersection on a Poincaré section. However, such intersection is very intricate, due in particular to the role of the LPO_1, as we shall show.

In order to simplify the exposition, let us start with the simplest EC orbits at P_1, involving the LPO_1. This means a trajectory that ejects from P_1, goes directly to the LPO_1 (that is, has $n = 0$ close passages around the primary), is a non transit orbit and turns back to collide with P_1 (after $j = 0$ close passages around the primary).

In order to find numerically such EC orbits, and guarantee the implication of the LPO_1, we just need to take into account a suitable set of initial angles θ_0 close to θ_0^1 and θ_0^2, that is ejection orbits passing close to the LPO_1, which are, moreover, non transit orbits (to guarantee the return towards P_1). This requirement leads us to take into account the heteroclinic connections H_0^1 and H_0^2.

More specifically we must intersect the curves $\gamma_{c,0}^1$ (collision orbits, integrated backward in time with $n = 0$, up to the first crossing with the section Σ^+) and either $\gamma_{e,0;l}^2$ or $\gamma_{e,0;r}^2$ (ejection orbits, integrated forwards in time with $n = 0$, and which we know they pass close to the LPO_1 and are *non transit*, up to the second crossing with the section Σ^+). We remark that we precisely select the pieces of $\gamma_{e,0;l/r}^2$, since we know they are non transit.

Let us focus on the intersection $\gamma_{e,0;r}^2 \cap \gamma_{c,0}^1$. See Figure 15 left ($(y, \dot{y})$ projection): the spiralling curves are plotted in green and $\gamma_{c,0}^1$ in blue. Each point belonging to the intersection of the green and blue curves is a point that belongs to an EC orbit (forward in time collides with P_1 and backward in time ejects from it and along its trajectory visits the LPO_1). So from the left plot, we see *apparently* two intersection points, that is two EC orbits. Let us denote by E_1 and E_2 these two *apparent* points that correspond (integrating forward in time) to collision orbits with initial angles $\theta_{0,c}^1$ and $\theta_{0,c}^2$, respectively. In Figure 15, E_1 and E_2 are the apparent intersection points with lower and higher value of $\dot{y}$ respectively. However, due to the heteroclinic connections H_0^1 and H_0^2, the green curve is an infinitely spiralling one, and this means that the *apparent* two points are actually a *double infinitely countable* set of intersection points, corresponding to a double infinitely countable set of values of initial angles θ_0 very close to an apparent value $\theta_{0,c}^1$ and $\theta_{0,c}^2$, respectively. Let us denote by C_∞^1 and C_∞^2 both sets of initial angles. Each infinity has to do with the infinity of spiral turns of the curve $\gamma_{e,0;l}^2$, and recall that this infinity of turns is related to the number of k turns (k from 0 to infinity) that the ejection orbit does around the LPO_1 (as discussed in the previous Section).

Considering $\gamma_{e,0;r}^2 \cap \gamma_{c,0}^1$, a double infinitely countable set of EC orbits is obtained. We observe that all these EC orbits share a common property: the ejection angle is very close to θ_0^1, so the initial path from ejection to (near) the LPO_1 looks quite the same as the path of H_1. Roughly speaking we will say that all these EC orbits have an "ejection road" type 1. Concerning the collision path, we will distinguish between those EC orbits with an intersection point, in $\gamma_{e,0;r}^2 \cap \gamma_{c,0}^1$, near E^1 or E^2. We will say that the EC orbit has a "collision road 1" or "collision road 2", respectively. So depending on the intersection point considered, we will have an infinity of EC orbits leaving from P_1 following the ejection road 1 and going to collision following the collision road 1 (if the intersection point belongs to C_∞^1); and an infinity of EC orbits leaving from P_1 following the ejection road 1 and going to collision following the collision road 2 (if the intersection point belongs to C_∞^2). For each infinity, the distinction between two EC orbits is simply the number of turns, k, around the LPO_1 after the ejection and before the collision.

Similarly we can think about $\gamma_{e,0;l}^2 \cap \gamma_{c,0}^1$. See Figure 15 middle with the same colour code. Now it is the heteroclinic orbit H^2 which plays a role. Roughly speaking we will say that all these EC orbits have an "ejection road" type 2, because the initial angle is close to θ_0^2. Again we distinguish the two collision roads 1 and 2, in accordance with the intersection point (see middle plot of Figure 15). So we obtain an infinity, $\tilde{C}_\infty^1$, of EC orbits leaving from P_1 following the ejection road 2 and collision road 1; and an infinity, $\tilde{C}_\infty^2$, of EC orbits leaving from P_1 following the ejection road 2 and collision road 2. Again, in both cases, the infinity appears because of the number k of turns around the LPO_1.

Therefore these four roads are the responsible for the existence of infinitely many EC orbits just choosing one "ejection road" and one "collision road", on the one hand, and taking into account the number of turns around the LPO_1, on the other hand. For each choice of the "ejection road" and "collision road" selected, we have an infinity of EC orbits with $n = 0$ close passages around P_1.

To illustrate some particular EC orbits, in Figure 16, we take three specific intersection points in $\tilde{C}_\infty^1$ that is in $\gamma_{e,0;l}^2 \cap \gamma_{c,0}^1$, corresponding to $k = 0, 1, 2$ turns around the LPO_1. The three of them take the "ejection road 2" and the "collision road 1" (see the top middle figure). We plot the associated EC orbits in the top right figure (orbit 1 with $k = 0$, bottom left figure (orbit 2 with $k = 1$) and bottom right figure (orbit 3 with $k = 2$). According to the code defined in the previous Section, such orbits are coded by: $E_1^0 - PO^0 - C_1^0$, $E_1^0 - PO^1 - C_1^0$ and $E_1^0 - PO^2 - C_1^0$, respectively.

Going on with some examples, taking $k = 0$ and the possible ejection road and collision road, we have four EC orbits shown in Figure 17. First row: two orbits with choice of ejection road 1 (left, due to $\gamma_{e,0;r}^2$), and either collision road 2 (orbit A in the middle) or collision road 1 (orbit B in the right). Second row: two orbits with choice of ejection road 2 (left, due to $\gamma_{e,0;l}^2$), and either collision road 2 (orbit C in the middle) or 1 (orbit D in the right, which coincides with Figure 16 bottom left). All of them coded by $E_1^0 - PO^0 - C_1^0$.

We want to emphasize that, so far, we have shown these four mechanisms (2 choices for the ejection road and 2 for the collision road) to explain the existence of the simplest EC orbit involving the LPO_1 with $n = 0$ (close passages from ejection to the LPO_1) and $j = 0$ (from the LPO_1 to collision arriving at collision after j close passages).

Of course, we can repeat the same kind of description for each given value of n and j. Regarding the number j, we plot in Figure 15 the curves obtained from collision with P_1, backwards in time up to Σ^+, for $l = 2$ (in red) and for $l = 3$ (in orange). The same four mechanisms apply again. For each ejection road and collision road chosen, we obtain an infinity of EC orbits (regarding the k turns around the LPO_1). Some particular examples are shown in Figure 17. We take $n = 0$ and $j = 2$ (third and fourth rows): orbit E (with ejection road 1, collision road 2), orbit F (with ejection road 1, collision road 1), orbit G (with ejection road 2, collision road 2), orbit H (with ejection road 2, collision road 1). All these orbits are coded as $E_1^0 - PO^0 - C_1^2$. Similarly we take $n = 0$ and $j = 3$ (fifth and sixth rows), EC orbits I, J , K and L, coded as $E_1^0 - PO^0 - C_1^3$.

5.2.2 EC orbits ejecting from P_1 involving the LPO_1 and colliding with P_2

An EC orbit ejecting from one primary (P_1 for instance) and colliding with the other primary (P_2) is a trajectory that belongs to $W^e(P_1) \cap W^c(P_2)$. So we will proceed in a similar way as in the previous subsection. In this case we will consider the intersection between the curve $\bar{\gamma}_{c,j}^1$ (the bar denoting collision orbits to P_2, integrated backward in time with j close passages around P_2, up to the first crossing with the section Σ^-) and $\gamma_{e,0;m}^2$ (ejection orbits from P_1, integrated forwards in time with $n = 0$, and that we know that pass close to the LPO_1 and are *transit* orbits, so we follow the orbits up to the second crossing with Σ_+). We remark that we precisely select the piece of $\gamma_{e,0;m}^2$, since we know they are transit orbits. We can see in Figure 15 right the curve $\gamma_{e,0;m}^2$, which is a double infinite spiral (in green) and $\bar{\gamma}_{c,j}^1$, for $j = 0$ (in blue), $j = 2$ (in red) and $j = 3$ (in orange). So, fixed n, the curve $\bar{\gamma}_{c,j}^1$ intersects $\gamma_{e,0;m}^2$ (the green one) in four infinitely countable sets of points (versus two infinite sets in the EC orbits to the same primary, as discussed in the previous subsection). Thus, we obtain four infinitely countable sets of ejecting orbits from P_1 and colliding with P_2. Similarly as before, the geometry of these orbits is determined through two ejection roads 1 and 2 (due to the double spiral) and two collision roads 1 and 2 (due to the intersection points). We show some particular examples ((x, y) projection) in Figure 18. First row: orbits coded as $E_1^0 - PO^0 - C_2^0$. Second row: $E_1^0 - PO^0 - C_2^2$. Third row: $E_1^0 - PO^0 - C_2^3$.

As above, these are the simplest orbits. We might take a value of n, a value of j and a value of k, to find a zoo of ejecting orbits from P_1 and colliding with P_2. However, in all the cases the geometrical mechanism is always the same.

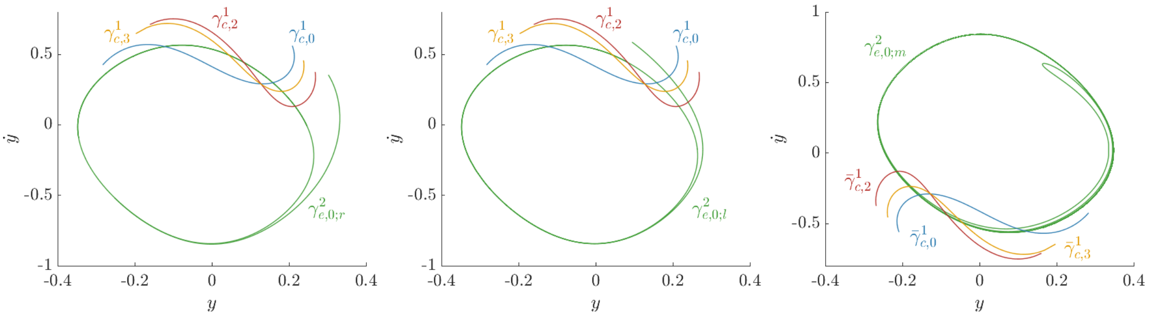

Figure 15: $\mu = 0.5$, $C = C_{L_2}$. (y, y') projection. Curves $\gamma^2_{e,0;i}$ (green) and $\gamma^n_{c,0}$, for $n = 0$ (blue), $n = 2$ (red), $n = 3$ (orange). Left. $i = r$. Middle. $i = l$. Each intersection point between the green curve and another one is a point of an EC orbit with P_1. Right. Curves $\gamma^2_{e,0;m}$ (green) and $\bar{\gamma}^1_{c,j}$, for $j = 0$ (blue), $j = 2$ (red), $j = 3$ (orange). Each intersection point between the green curve and another one is a point of an EC orbit (ejects from P_1 and collides with P_2).

6 Global evolution and detection of ejection-collision orbits

Our main goal in this Section is to provide a plot that contains the description of the dynamics of any ejection orbit, for a given finite range of time. That is, we provide a plot containing the dynamics of the set of ejection orbits from a global point of view. Thus, naturally, we should present a 3D-plot containing the dynamical information in the variables x, y and time. But this turns out to generate very heavy loaded plots. Instead, we will use lighter 2D plots with colours containing 3D information. We call them *colour diagram plots*. Roughly speaking, the whole motivation and goals of the paper are provided in these colour diagram 2D plots in Figures 22 and 23. We will discuss the effect that the variation of C has on the dynamics on the ejection orbits, and, of course, we will recover the information described in the previous Sections concerning transition intervals I_n and chaos.

So, for a value of $\mu \in (0, 1)$ given, the particle ejects from the big ($\mu \in (0, 0.5]$) or small primary ($\mu \in (0.5, 1)$) and we fix a value of C. Since we are particularly interested in the influence of the LPO_1 and their manifolds on ejection orbits, we will consider (as in the previous sections) values of $C \geq C_{L_{2,3}}$.

But before providing directly such diagram plots and their description, we discuss first two items which should be understood independently and that afterwards, will appear as part of the diagram plots. We think they will help the reader to easier interpret and understand the meaning of such 2D plots.

(i) *Time to reach the successive minima distances to a primary.* We want to illustrate the effect of decreasing C (for μ fixed) on the time needed to make an excursion from ejection until the next passage at minimum distance with respect to a primary. To do so we compute the normalized time to reach the k-th close approach to the primary as a function of the initial ejection angle, that is, for a given μ and C fixed, we compute

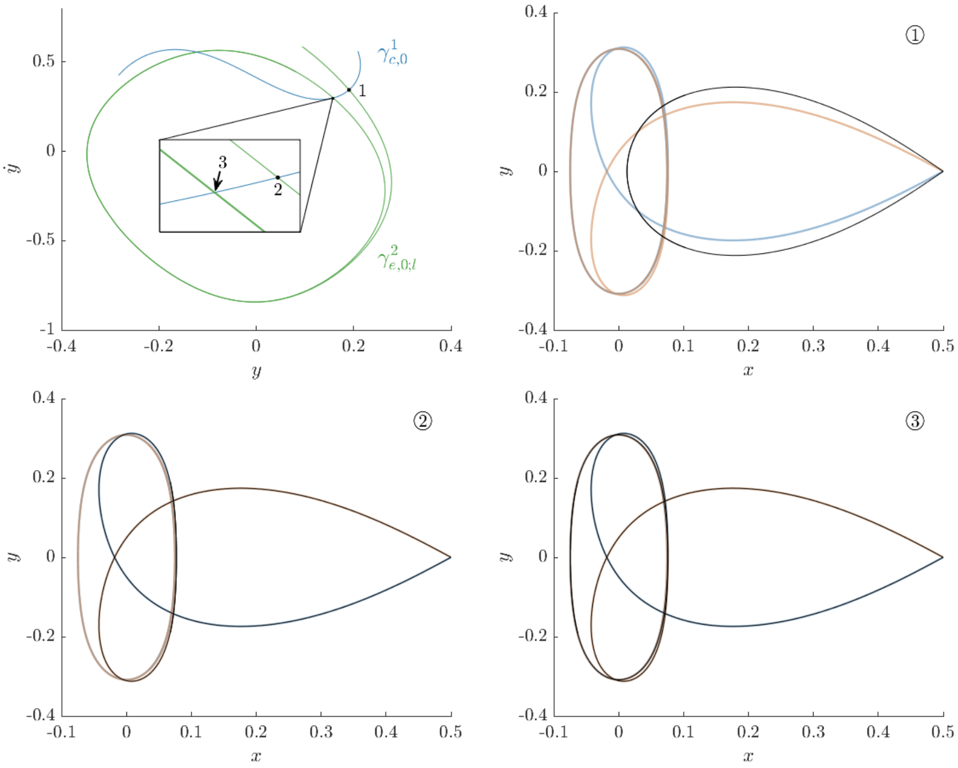

Figure 16: $\mu = 0.5$, $C = C_{L_2}$. Top left. $(y, \dot{y})$ projection. Curves $\gamma^2_{e,0;l}$ and $\gamma^1_{c,0}$. We choose three intersection points corresponding to $k = 0, 1, 2$ turns around the LPO_1. The three of them take the "ejection road 2" and the "collision road 1". We plot the associated EC orbits (black path) with $k = 0$ (orbit 1, top right), $k = 1$ (orbit 2, bottom left) and $k = 2$ (orbit 3, bottom right). (x, y) projection. The blue and red orbits correspond to the heteroclinic connections H_1 and H_2 respectively.

$$T_k^N(\theta_0) = \frac{T_k(\theta_0)}{\bar{T}_k}$$

where $T_k(\theta_0)$ is the necessary time to reach the k-th minimum distance to the primary for that θ_0 and $\bar{T}_k$ is the mean value obtained from all the values of T_k varying θ_0, that is, the mean time that the ejection orbits need to reach the k-th minimum distance.

We plot in Figure 19 top the curves obtained for $T_k^N(\theta_0)$ for $k = 1, ..., 10$ and different values of C. On the x-axis we put the k-th close approach, and on the y-axis the initial ejection angle θ_0. The green curve corresponds to $C = 10$, the blue one to $C = 5$, the black one to $C = 4.2$ and the red one to $C = 3.8$. Two aspects should be mentioned. First, as expected, for an ejection angle θ_0 close to $\pi/2$, since the ejection velocity points towards the other primary, the influence of this other primary is apparent, not only for big values of $k \geq 4$ but also for small ones. For small values of k, we see almost vertical curves with a clear deviation (maximum in time) for θ_0 near $\pi/2$. See Figure 19 (top) for $k = 1, 2, 3$. In particular, for $k = 1$, we plot in the figure a zoom area and by a dot we remark the time to reach the maximum time of the curves $T_1^N(\theta_0)$, for the four different values of C. In the bottom figure, we plot the corresponding ejection orbits (for the four particular values of θ_0), in the (x, y) variables, for the range of time that it takes to reach the first minimum (in continuous line) and a bit more (in discontinuous line). We observe how the shape of the ejection curve changes close to the minimum when decreasing C. For bigger values of k, the deviation, when θ_0 is near $\pi/2$, is clearly more visible and the time to reach the k-th minimum distance gets longer. See the top figure for $k \geq 7$. Second, when C decreases and k increases, the curves for each k look like waves with

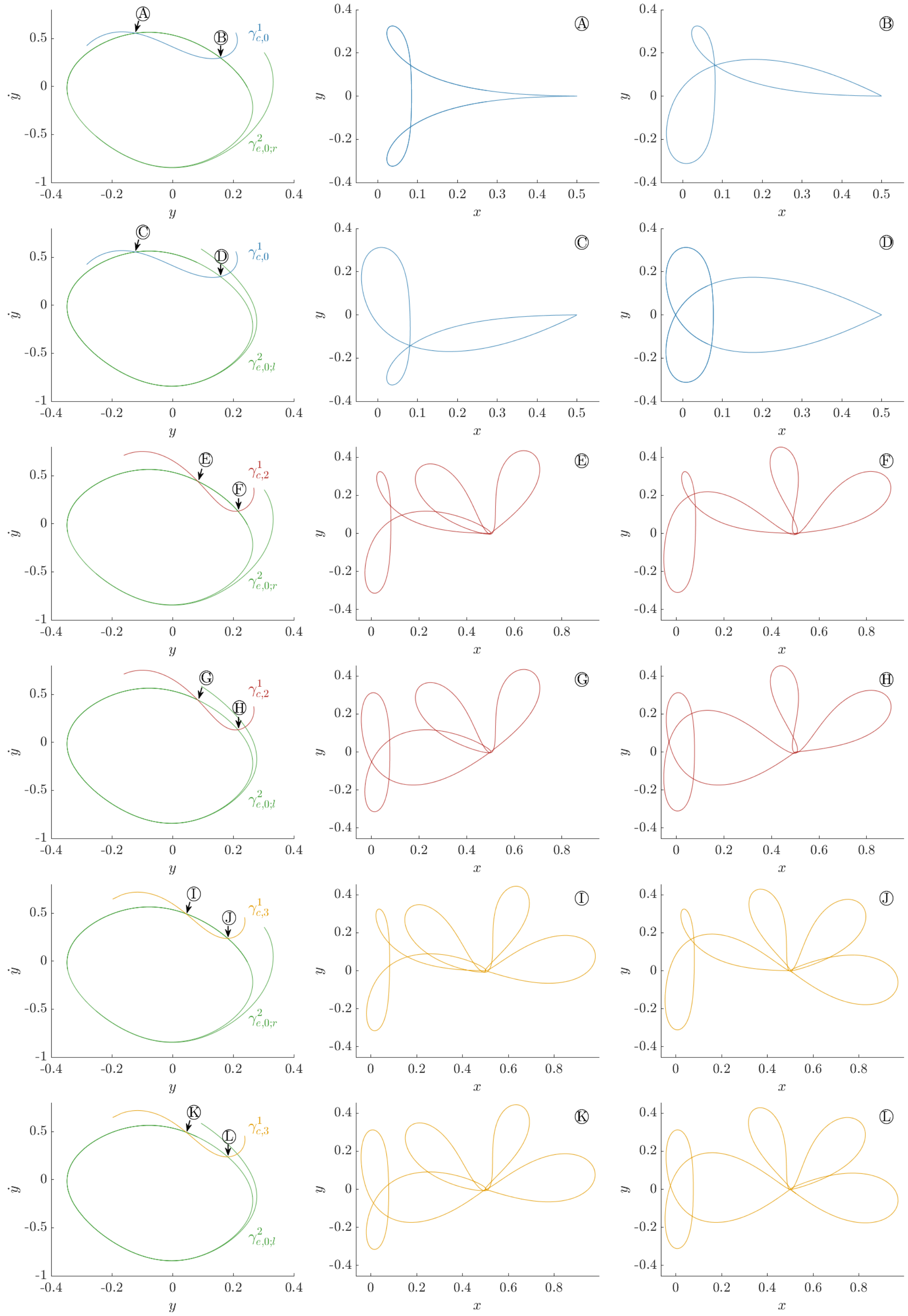

Figure 17: $\mu = 0.5$, $C = C_{L_2}$. Left. Curves $\gamma^2_{e,0,r/l}$ and $\gamma^1_{c,n}$ (left column) $(y, \dot{y})$ projection. Middle and right columns, (x, y) projection. $n = 0$, first and second rows. Orbits $E^0_1 - PO^0 - C^0_1$. $n = 2$, third and fourth rows. Orbits $E^0_1 - PO^0 - C^2_1$. $n = 3$, fifth and sixth rows. Orbits $E^0_1 - PO^0 - C^3_1$.

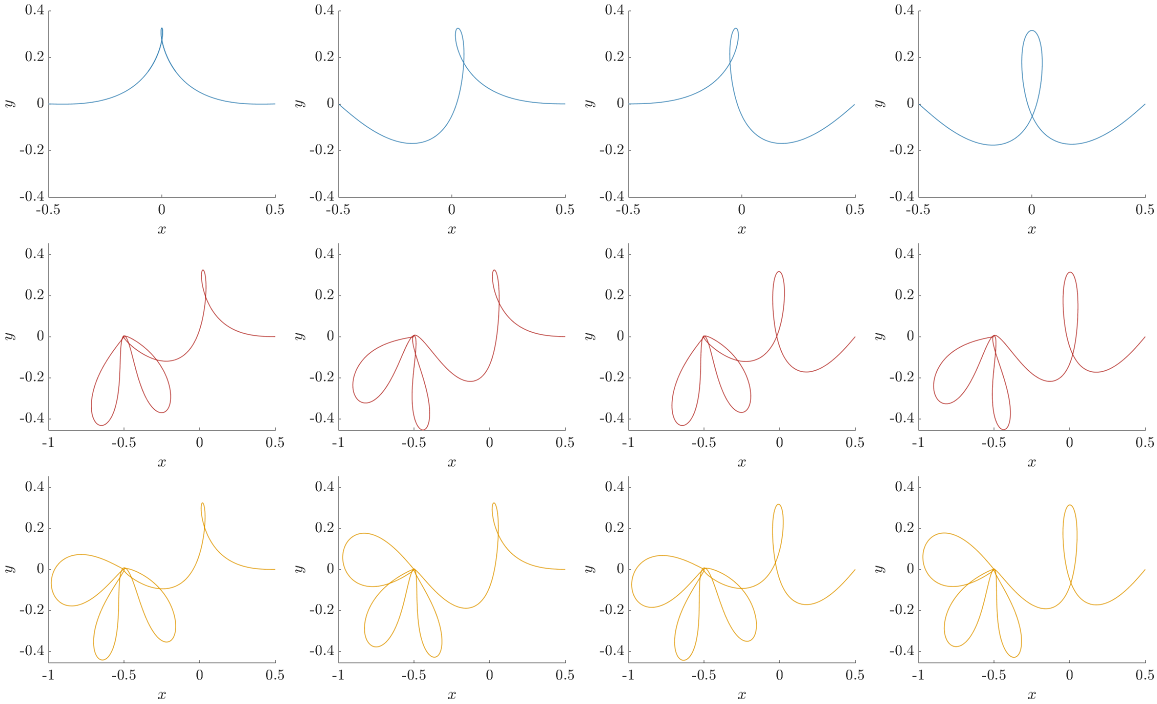

Figure 18: $\mu = 0.5$, $C = C_{L_2}$. Some orbits ejecting from P_1 and colliding with P_2. (x, y) projection. First row: orbits coded as $E_1^0 - PO^0 - C_2^0$. Second row: $E_1^0 - PO^0 - C_2^2$. Third row: $E_1^0 - PO^0 - C_2^3$.

several ripples. It is clear that as C decreases, the amplitude of the LPO_1 gets bigger, and its stable and unstable manifolds play also some role on the trajectory of the ejecting orbits giving rise to such ripples. Actually this is consistent with the description done in the previous sections.

(ii) *System of coordinates used and particular examples.* In order to understand the system of coordinates used, we divide the bounded Hill region in two regions separated by the line $x = x_{L_1}$. We use polar coordinates (r, θ) (instead of cartesian ones (x, y)) at each region around the corresponding primary which is at the origin of this system of coordinates. Each region has a colour, blue for the region around the right primary and red for the one around the left primary. Actually we will use a shaded gradual colour to identify the angle θ, and the contour level curves also in a shaded gradual colour will identify the distnace r to the primary. In Figure 20 we show an image for $C = C_{L_2}$ and $\mu = 0.3$ (left), $\mu = 0.5$ (middle) and for $C = C_{L_3}$ and $\mu = 0.8$ (right). As shown in the plots, an angle of θ near 0 (near 2π) corresponds to dark blue (light blue), in the region around P_1. Similarly we use orange (dark red) in the region around P_2. On the other hand, the darker (lighter) the contour lines are, the closer (further) the particle is from the corresponding primary.

So the important point is to visualize the dynamical behaviour of an orbit (and particularly an ejection orbit), along time, through colours. In Figure 21 we show three different examples of orbits and its evolution in the range of time $[0, 5]$, both in cartesian coordinates and the corresponding colour code band. The first example corresponds to an ejection orbit (in blue). In (x, y) coordinates the trajectory is self explanatory. The number labels on the trajectory correspond to the location of the particle at the precise instants of time $t = 1, 2, 3, 4, 5$. When regarded according to the colour code band (first one in the bottom figure), we observe the following: since the colour is always blue, the ejecting particle from P_1 remains in that region; from $t = 0$ to $t = 2$, and from $t = 4$ to $t = 5$ the angle crosses the line $\theta = 0$, and the vertical lines provide information about the distance from the particle to P_1. We see vertical darker lines when the particle is closer to the primary, and the bands with a similar intensity of blue correspond to the upper or lower half plane. Regarding the second example, the red orbit in (x, y) coordinates lives in the region around P_2. We can see the close and far passages around P_2 through the vertical lines and the successive passages of the angle through $\theta = 0$, from the sudden changes from lightest orange to darkest red. Finally, the third example corresponds to an orbit that transits from the region around P_1 to the region around P_2. This is clearly seen on the third colour code band, from $t = 0$ to close to $t = 1$: we infer the behaviour of the particle on the region around P_1, from the blue colour and its varying intensity. Then the sudden change from blue to orange corresponds to a transition from one region to the other one. From now on, the intensity in red and the vertical lines describe the trajectory of the particle in that region as time passes by.

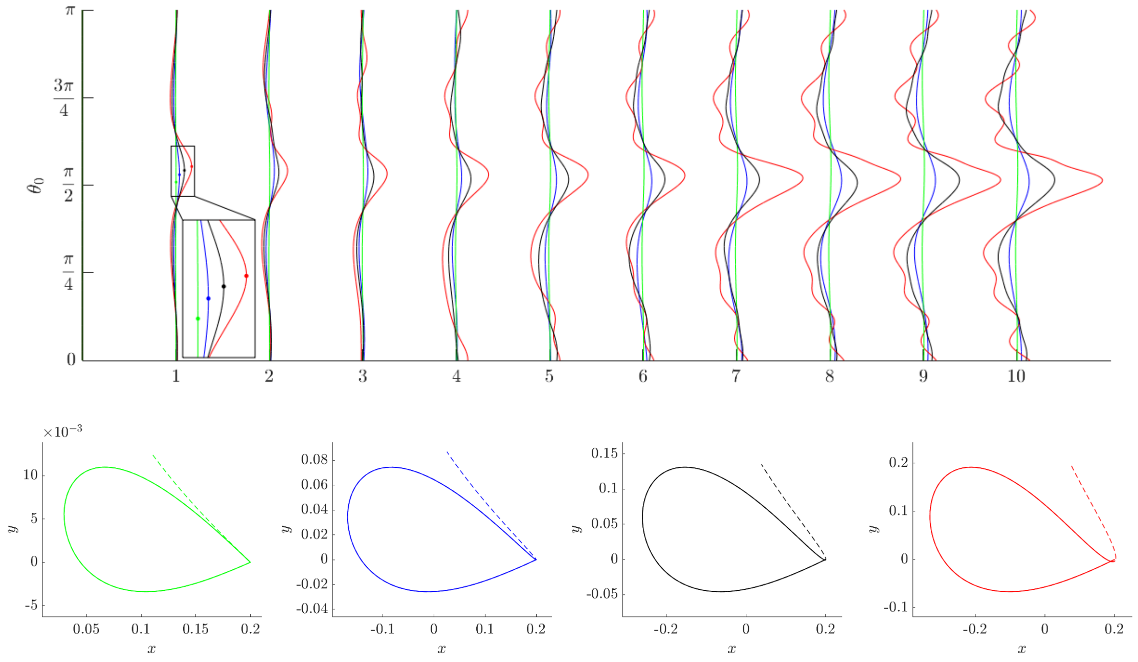

Figure 19: $T_k^N(\theta_0)$ at the k-th minimum distance with the primary for $\mu = 0.2$. The green curve corresponds to $C = 10$, the blue one to $C = 5$, the black one to $C = 4.2$ and the red one to $C = 3.8$.

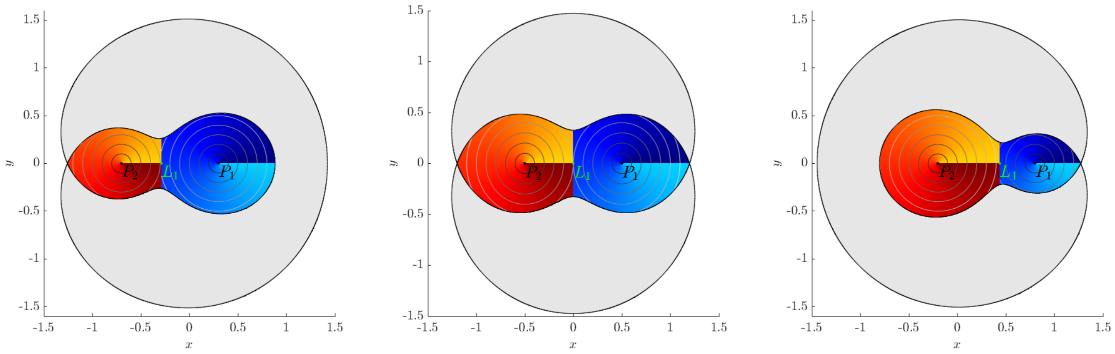

Figure 20: Bounded Hill region and identification of the two separate regions, one around each primary. $C = C_{L_2}$ and $\mu = 0.3$ (left), $\mu = 0.5$ (middle). $C = C_{L_3}$ and $\mu = 0.8$ (right).

Now, let us proceed to an important point of the paper and that somewhat collects and reflects the results discussed in the previous sections: the *description of the colour diagram plots*. After explaining the colour code to follow the actual trajectory of any particular ejection orbit (as done in the previous item (ii)), we have done massive simulations in order to obtain the complete colour code diagrams for different values of $\mu \in (0, 1)$ and varying C.

For example, we provide the colour code diagrams in Figure 22 for $\mu = 0.5$, and different values of C

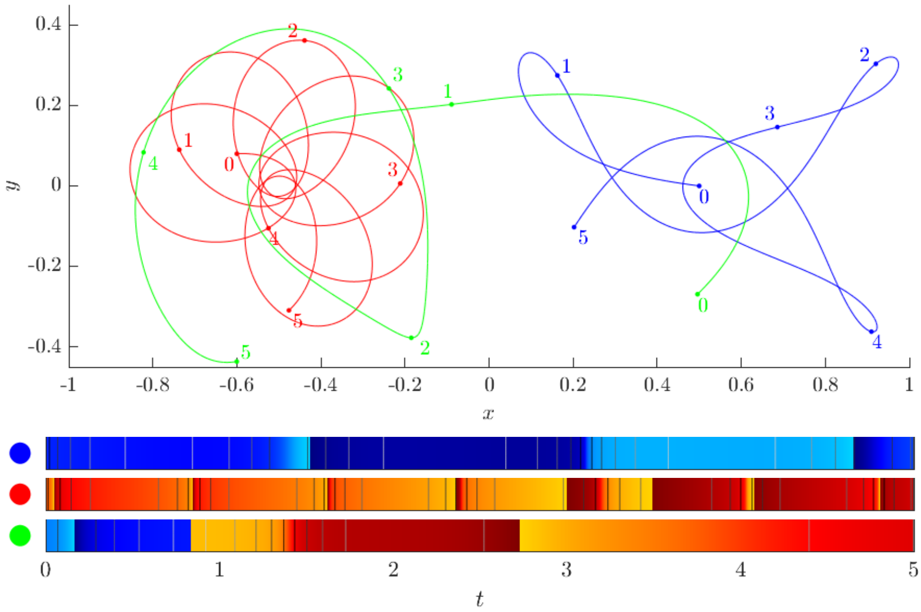

Figure 21: Three different examples of orbits in (x, y) coordinates (top) and the associated colour code (bottom), for $t \in [0, 5]$. Number labels are added to identify easily the actual geometrical path with the colour in the diagrams.

to see the effect of varying C for a μ given; and in Figure 23 for $C = C_{L_2}$ and different values of μ to see the effect varying μ for $C = C_{L_2}$ given. In all cases the range of time $t \in [0, 10]$.

Let us start with Figure 22. We show the colour code diagrams obtained for $\mu = 0.5$ and $C = C_{L_1} = 4.25, 4.1, 4, 3.85, C_{L_2} = 3.7067962240861525$ and range of time $t \in [0, 10]$ (from top to bottom). Notice that on the y-axis, we also add the transition intervals I_n (range of values of θ_0 for which there is transition from one region to the other one), discussed in Section 4. We keep the same colour used in Figures 8 and 9: blue, red and brown for $n = 0$, $n = 2$ and $n = 3$ ejection orbits, respectively. Recall that n allows to classify the ejection orbits since it is the number of close passages that the ejection orbit describes after ejection, and the endpoints of each interval (that give rise to heteroclinic connections $P_i - LPO_1$ are the frontier between two regimes, transit to the region around the other primary or remaining in the same region the particle ejected from. As discussed in Section 4, such transition intervals appear depending on μ and C, for n given. That is the reason why in the figure only such intervals appear in the last two plots. Now let us explain each plot in the Figure 22.

For $C = C_{L_1} = 4.25$, the bounded motion takes place in each independent Hill region around the primary, so any ejection orbit remains on this region for ever. See Figure 22 first row. For a given θ_0, the particle ejects form P_1, does the successive far and close passages around the primary P_1 (visible by the darker successive curves). This first plot is related to the top one of Figure 19. If we decrease the value of C just a bit, for example $C = 4.1$, there is a very narrow channel that communicates the region around P_1 and the region around P_2. Although there exists the LPO_1 with a small amplitude as well as its invariant stable and unstable manifolds, their influence has no apparent effect for this range of time (we would see its effects for longer ranges of time). So we do not see yet any ejecting orbit that transits to the region around P_2. See Figure 22 second row. For $C = 4$, the channel is wider and so is the LPO_1. So now the transit passage from one region from one region to the other one is more feasible. We observe in Figure 22 third row the two thin tongues of transit orbits that have appeared, clearly seen by the change of colour from blue to orange. Now for a value of θ_0 in between these two tongues, we can easily describe the corresponding ejection orbit. For example, if we take θ_0 in the first tongue (values of $\theta_0 < \pi/2$), we see that the particle, after ejecting from P_1 and describing six close passages around this primary (seen as six darker blue wave deformed vertical curves), transits to the region around P_2 (entering through the region $x < 0, y > 0$, –orange colour–), describes one turn around P_2 (colour changes from orange to red) and transits again to the region around P_1 (blue colour).

For $C = 3.85$, see Figure 22 fourth row, the channel gets wider now and there is a tongue of transit orbits, which appears for t less than the unity (see the orange tongue in the figure). For such orbits, the particle ejects from the primary P_1, has $n = 0$ close approaches to P_1 and transits to the region around P_2 (look at the change of colour from blue to orange approximately in the central part of the plot). The blue transition interval (on the y axis) $I_0 = (\theta_0^1, \theta_0^2)$ (for $n = 0$) (according to the notation of Section 3) is also plotted. We know that for the values of θ_0^1 and θ_0^2 endpoints of I_0 we have heteroclinic connections which are responsible for the chaotic motion if we take values of θ_0 close to both of them (due to the existence of many heteroclinic connections $P_1 - LPO_1$). This can be checked on the plot where many changes of colour are clearly visible. For values of θ_0 in the central part of interval, the path of the trajectories can still be distinguished (for $t \in [0, 7]$), whereas for values of θ_0 near θ_0^i, $i = 1, 2$, we see chaotic behaviour (that is, very thin tongues non distinguishable).

Finally for $C = C_{L_2}$, the channel is yet wider, and there appear new sets of transit orbits, clearly visible from the change of blue colour to red/orange in the plot. See Figure 22 last row. Of course, these transitions are in accordance with the intervals I_n, for $n = 0, 2, 3$, also plotted on the y-axis. Remark that simply looking at the plot (the deformed darker vertical waves), we can count the number n of close approaches before the transition ($n = 0$ for the blue interval, $n = 2$ for the red one and $n = 3$ for the brown one).

Now let us move to the next figure and discuss the global evolution of the ejection orbits, not in terms of variation of C, for μ fixed, but with respect to μ, for a C fixed. We will consider $C_{L_{2,3}}$ (see Figure 20) where both the channel between the regions around each primary and the amplitude of the LPO_1 are maxima. We remark, however, that the size of the channel and the amplitude increase with μ. In Figure 23 we plot the colour diagrams for the values of $\mu = 0.2$, 0.3, 0.7, 0.8, 0.9 (from top to bottom plots). It is clear from the pictures that for moderate values of μ ($\mu = 0.2$ on the first row plot) the particle that ejects from the big primary P_1 does not feel enough attraction from the small primary and the LPO_1 is also small, so the particle, for this range of time, remains on the region around P_1. However, when μ increases, as expected, the particle feels the attraction of the other primary, and since the LPO_1 is bigger, it is easier to have ejection orbits that transit to the other region. In a natural way, there appears a main tongue of transit orbits for θ_0 near $\pi/2$. Again we have plotted the transition intervals I_n, $n = 0, 2, 3$ on the y-axis, as particular examples. A final remark is that just looking at these diagrams, not only we recognise the I_n intervals, for $n = 0, 2, 3$, but we easily identify other transition intervals. For example see the interval I_5 (not labelled on the y-axis) on second row plot: we can see the horizontal tongue on the approximate central part of the plot for an interval of time $[0, 6]$; for each value of θ_0 in this interval, the corresponding ejection orbit crosses five deformed darker vertical curves, each one associated to a close passage to P_1.

Just to end this Section, and after the above discussion of the evolution of the ejection orbits, from the ejection instant up to $t = 10$, focussing on successive transitions and close passages to one primary, let us concentrate on a particular type of ejection orbits: the *Ejection-collision orbits*. More specifically, let us explain how to visualize two cases: first, ejection-collision orbits with a primary and, second, ejection from one primary and collision to the other one.

So first, let us focus on the EC orbits with a primary. We show in Figure 24 a zoom area for $t \in [0, 5]$ and $\theta_0 \in [0.7, 1.5]$, $\mu = 0.5$ and $C = C_{L_2}$ where we distinguish two values of θ_0 for which we obtain two EC orbits with the big primary. We label the collision points by C_1 and C_2 on the diagram. Of course, concerning the two top plots, we have the same information taking into account the usual time t or the local Levi-Civita time s_1. However, we remark the advantage of using s_1 instead of t: the thin transition of blue colour using t (the left plot) is widened taking the time s_1 and therefore the transition is more clearly visible. Let $\theta_{0,c}$ be the specific value for the EC orbit that collides at C_1. We know that $d\theta/ds$ will be zero at the instant of collision. Moreover, for two different values of θ_0, one bigger and the other one smaller than $\theta_{0,c}$, we know that $d\theta/ds$ will change sign, at the minimum distance to the primary. This change of sign is precisely what we show in the plot: for the three orbits, blue, red (EC orbit) and green (in the bottom left figure), we see this change of sign close to the collision, that is the particle passes on one side (for the blue orbit) or the other one (for the green orbit) with respect to the primary. Similarly, in the top figure, we take the three initial values of θ_0 labelled by the same small colour arrows, and we follow for each θ_0 the corresponding ejection orbit along time. For a range of time s_1 near the time of collision at C_1, we see the degradation of blue colour that goes from dark blue to light one for $\theta_0 < \theta_{0,c}$ and from light blue to dark one for $\theta_0 < \theta_{0,c}$. In between we take the $\theta_{0,c}$ value and on the same range of time, we see that the orbit after and before the collision remains on the same colour region (dark blue in the top figure). A completely analogous behaviour is observed for the collision at C_2. Now the orbits are coloured purple, orange and dark green.

Second and finally, concerning the EC orbits that eject from one primary and collide to the other one, a similar description is obtained. In Figure 25, we consider $\mu = 0.5$ and $C = C_{L_2}$, and show the evolution of five ejection orbits, purple, green (EC orbit), orange, blue (EC orbit) and red. Of course, in the colour code diagram, the ejection orbits start at the blue region (because they ejct from P_1), but move to the other region (change of colour from blue to orange or dark red). We can distinguish the collision because if we take a small box containing on its center C_1 (and not containing C_2) on the right plot, then varying θ_0 on this box from top to bottom, we see the degradation from orange to red above C_1 (look at the orange orbit that describes an increasing angle –in polar coordinates– close to the collision); we observe a degradation from red to orange under C_1 (look at the yellow orbit that describes a decreasing angle –in polar coordinates– close to the collision). Therefore, necessarily there must exist a collision in between (look at the blue EC orbit at C_1). A similar reasoning applies to a small box containing C_2 (and not C_1). Now we can consider the yellow, green (collision) and purple orbits.

7 Conclusions

From the numerical simulations done, we can conclude that there is a rich variety of behaviours as far as ejection orbits are concerned. In the range interval $C \in [C_{L_{2,3}}, C_{L_1}]$, such richness is explained from the LPO_1 and its invariant stable and unstable manifolds that do interact with the ejection orbits. In particular, the many infinities of homoclinic orbits to LPO_1 give rise to a rich generation of also many infinities of heteroclinic connections $P_1 - LPO_1$ that at the same time have a direct effect on the classification of the dynamical trajectory of the ejection orbits (taking into account the number of close approaches to one primary and the transit/non transit property). A final conclusion is that, given μ and C, suitable two dimensional plots (instead of 3 dimensional heavier ones) can be generated in order to have a global picture of the dynamical behaviour of the whole set of ejection orbits for a finite range of time.

8 Acknowledgements

M. Ollé and O. Rodríguez were supported by the Spanish MINECO/FEDER grant PGC2018-100928-B-100 and the Catalan grant 2017SGR-1049. J. Soler was supported by MTM2016-77278-P.

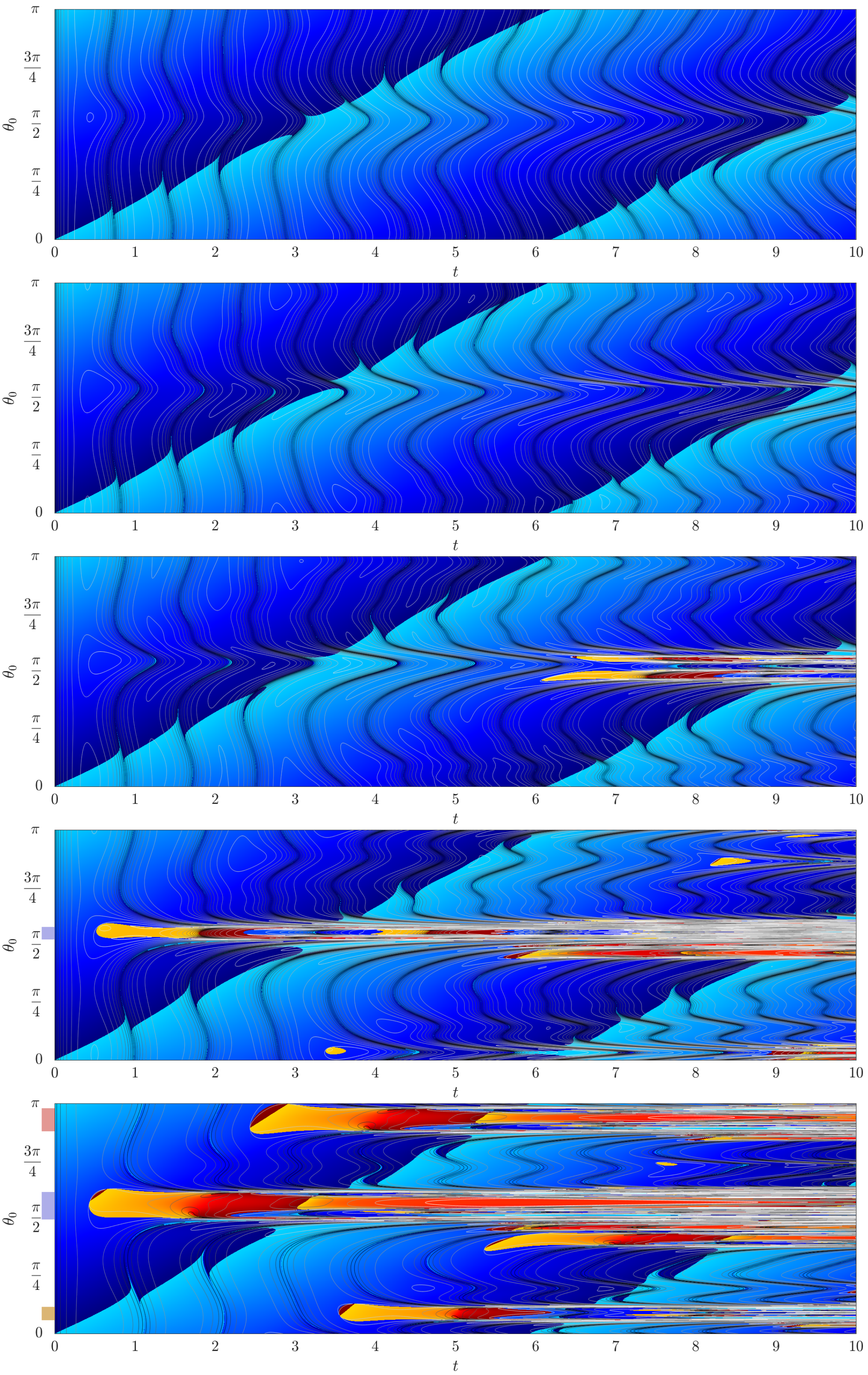

Figure 22: Colour code diagrams for $\mu = 0.5$ and $C = C_{L_1}, 4.1, 4, 3.85, C_{L_2}$ (from top to bottom). On the y-axis, we add the transition intervals I_n: blue, red and brown for $n = 0$, $n = 2$ and $n = 3$ ejection orbits, respectively. See more explanation in the text.

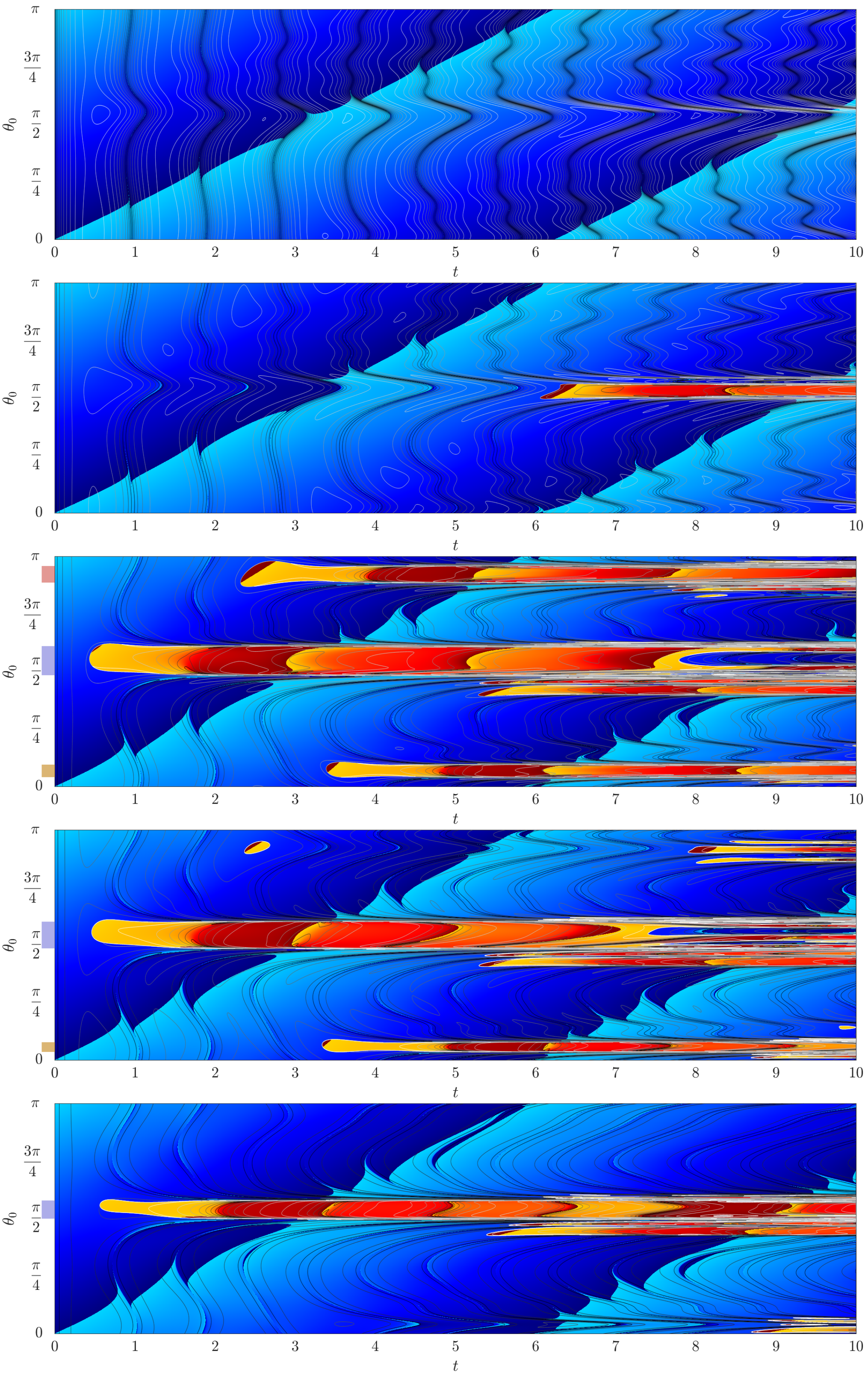

Figure 23: Colour code diagrams for $C = C_{L_2}$ and $\mu = 0.2$, 0.3, 0.7, 0.8 and 0.9 (from top to bottom). On the y-axis, we add the transition intervals I_n: blue, red and brown for $n = 0$, $n = 2$ and $n = 3$ ejection orbits, respectively. See more explanation in the text.

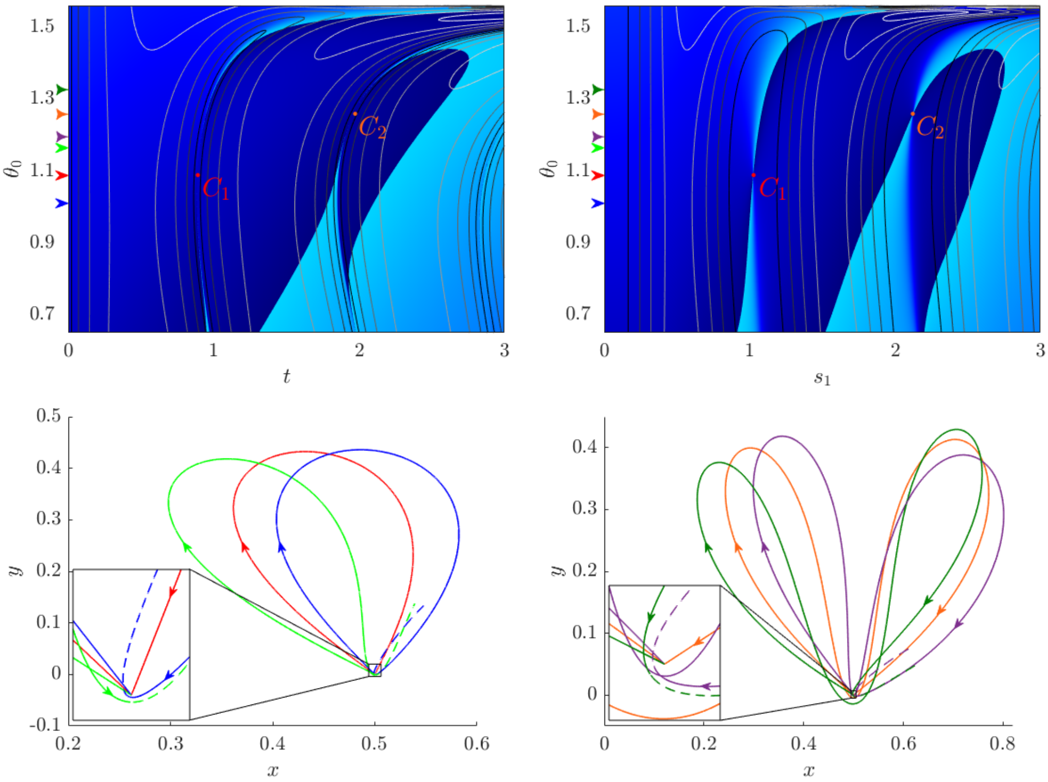

Figure 24: Top. Zoom of a colour code diagram to visualize two different EC orbits, the collision taking place at C_1 and C_2 respectively. On the x axis, the usual time t (left) and Levi-Civita time s_1 (right). Bottom. (x, y) variables. We plot the two EC orbits and two orbits nearby to show the path close and at collision. Increasing θ_0 compare the blue and green ejection orbits, with the red EC orbit C_1 in between; and similarly, the purple and dark green orbits with the orange EC one C_2 in between. The values of θ_0 for these orbits are indicated, with the same colour, in the ordinate axis of the top figures.

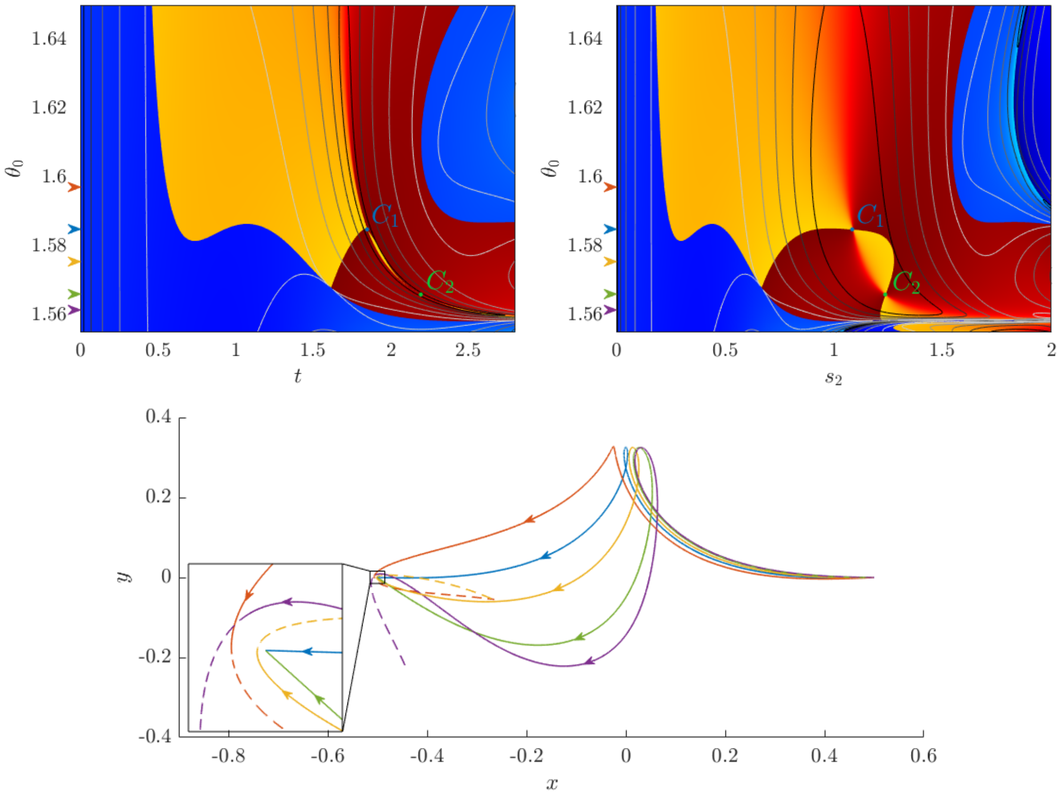

Figure 25: Top. Zoom of a colour code diagram to visualize two different orbits, that eject from P_1 and collide with P_2, the collision taking place at C_1 and C_2 respectively. On the x axis, the usual time t (left) and Levi-Civita time s_1 (right). Bottom. (x, y) variables. We plot five ejection orbits to show the path close and at collision. Decreasing θ_0 compare the orange and yellow ejection orbits, with the blue EC orbit in between; and similarly, the yellow and purple orbits with the green EC one in between. The values of θ_0 for these orbits are indicated, with the same colour, in the ordinate axis of the top figures.

References

[1] Astakhov, S. A., Burbanks, A. D., Wiggins, S., Farrelly, D., Chaos-assisted capture of irregular moons. Lett. to Nature 2003;423:264–267.

[2] Astakhov, S. A., Lee, E. A., Farrelly, D., Formation of Kuiper-belt binaries through multiple chaotic scattering encounters with low-mass intruders. Mon. Not. R. Astron. Soc. 2005;360:401–415.

[3] Barrabés, E., Mondelo, J. M., Ollé, M., Numerical continuation of families of heteroclinic connections between periodic orbits in a Hamiltonian system, Nonlinearity 2013;26:2747–2765.

[4] Bozis, G. Sets of collision periodic orbits in the Restricted problem. In: Periodic orbits, stability and resonances, G.E.O. Giacaglia (eds). Holland: D. Reidel Pub. Co.; 1970, p. 176–191.

[5] Brunello, A. F.,Uzer, T., Farrelly, D. Hydrogen atom in circularly polarized microwaves: Chaotic ionization via core scattering. Phys Rev A 1997;55:3730–3745.

[6] Chenciner, A. and Llibre, J. A note on the existence of invariant punctured tori in the planar circular RTBP. Ergod. Th. & Dynam. Sys. 1988;8:63–72.

[7] Devaney, R. L. Singularities in Classical Celestial Mechanics. In: Ergodic Theory and Dynamical Systems I, Proceedings Special year, Maryland 1979-80, A. Katok (Ed.), p. 211–333.

[8] Dormand, J.R. and Prince, J.P. A familiy of embedded Runge-Kutta formulae. J. Computat. App. Math., volume 6, n 1, 1980.

[9] Erdi, B., Global regularization of the Restricted Problem of three bodies. Celest Mech Dyn Astron 2004;90:35–42.

[10] Hénon, M., Exploration numérique du problème restreint I. Masses égales, Orbites périodiques. Ann Astrophys 1965;28:499–511.

[11] Hénon, M. Numerical exploration of the Restricted Problem V. Hill's case: Periodic orbits and Their Stability. Astron Astrophys 1969;1:223–238.

[12] Hurley, J. R., Tout, C. A., Pols, O. R. Evolution of binary stars and the effect of tides on binary populations Author Notes. MNRAS J. 2002;329(4):897–928.

[13] Jorba, A. and Zou, M. A software package for the numerical integration of ODE's by means of high-order taylor methods. Exp Maths 2005;14:99–117.

[14] Lacomba, E. A. and Llibre, J. Transversal Ejection-Collision Orbits for the Restricted Problem and the Hill's Problem with Applications. J Differ Eq 1988;74:69–85.

[15] Llibre, J. On the Restricted Three-Body Problem when the Mass Parameter is Small. Celest Mech Dyn Astron 1982;28:83–105.

[16] Llibre, J, and Martinez-Alfaro, J. Ejection and collision orbits of the spatial RTBP. Celest Mech Dyn Astron 1985;35:113–128.

[17] Llibre, J. and Pinyol, C. On the Elliptic Restricted Three-Body Problem. Celest Mech Dyn Astron 1990;48:319–345.

[18] Meyer, K. R., Offin, D. C. Introduction to Hamiltonian Dynamical Systems and the N-Body Problem. Springer, Switzerland; 2017.

[19] Modisette, J. L., Kondo, Y. Mass Transfer between Binary Stars. Symposium - International Astronomical Union 1980, Vol. 88.

[20] Nagler, J., Crash test for the Copenhaguen problem. Phys. Rev. E 2004;69:066218.

[21] Nagler, J., Crash test for the restricted three-body problem. Phys. Rev. E 2005;71:026227.

[22] Ollé, M. To and fro motion for the hydrogen atom in a circularly polarized microwave field. Commun Nonlinear Sci Numer Simulat 2018;54:286-301.

[23] Ollé, M., Rodríguez, O., Soler, J. Ejection-collision orbits in the RTBP. Commun Nonlinear Sci Numer Simulat 2018;55:298-315.

[24] Ollé, M., Rodríguez, O., Soler, J. Regularization in ejection-collision orbits of the RTBP. Recent Advances in Pure and Applied Mathematics, RSME Springer Series 4, 2020.

[25] Ollé, M., Rodríguez, O., Soler, J., Analytical and numerical results on families of n-ejection-collision orbits in the RTBP. Commun Nonlinear Sci Numer Simulat 2020;90:105294.

[26] Paez, R.I.; Guzzo, M., A study of temporary captures and collisions in the Circular Restricted Three-Body Problem with normalizations of the Levi-Civita Hamiltonian. Preprint 2020.

[27] Pinyol, C. Ejection-collision orbits with the more massive primary in the planar elliptic restricted three-body problem. Celest Mech Dyn Astron 1995;61:315–331.

[28] Pringle, J. E., Wade R. A. Interacting Binary Stars. Cambridge Univ. Press, Cambridge; 1985.

[29] Stiefel, E. L., Scheifele, G. Linear and regular Celestial Mechanics. Springer-verlag, New York; 1971.

[30] Szebehely, V. Theory of orbits. Academy Press, Inc., New York; 1967.

[31] Witjers, R.A., Davies, M. B., Tout, C. Evolutionary processes in binary stars. Proceedings of the NATO ASI on evolutionary processes in binary stars, Cambridge, UK, July 10-21, 1995.